2017-03-01

Extension of the QuikSCAT Sea Ice Extent Data Set with OSCAT and ASCAT Data

Jordan Curtis Hill
Brigham Young University

Extension of the QuikSCAT Sea Ice Extent Data Set with OSCAT and ASCAT Data

Jordan Curtis Hill

A thesis submitted to the faculty of
Brigham Young University
in partial fulfillment of the requirements for the degree of

Master of Science

David G. Long, Chair
Brian A. Mazzeo
Wood Chiang

Department of Electrical Engineering

Brigham Young University

ABSTRACT

Extension of the QuikSCAT Sea Ice Extent Data Set with OSCAT and ASCAT Data

Jordan Curtis Hill
Department of Electrical Engineering, BYU
Master of Science

Polar sea ice measurements are an important contribution to global climate models. Passive and active microwave remote sensing instruments are used to track global trends in polar sea ice growth and retreat from day to day. A scatterometer sea ice extent data set is valuable for comparison with other radiometer data sets and ground based measurements. This scatterometer sea ice record began with the NASA Scatterometer (NSCAT) and continued with the Quick Scatterometer (QuikSCAT) data set.

The Ku-band Oceansat-2 scatterometer (OSCAT) is very similar to the Quick Scatterometer, which operated from 1999 to 2009. OSCAT continues the Ku-band scatterometer data record through 2014 with an overlap of eighteen days with QuikSCATs mission in 2009. This thesis discusses a particular climate application of the time series for sea ice extent observation. In this thesis, a QuikSCAT sea ice extent algorithm is modified for OSCAT. Gaps in OSCAT data are accounted for using a reverse time processing approach. The data gaps are filled in to support sea ice extent mapping. The data set is validated with overlapping data from QuikSCAT as well as the sea ice extent data set calculated from Special Sensor Microwave Imager data by the NASA Team algorithm.

Data from the Advanced Scatterometer (ASCAT), which operates at C-band, are processed using a Bayesian classification algorithm for a stand-alone C-band sea ice extent product to continue scatterometer sea ice extent observation past 2014. ASCAT azimuth dependence data is developed for use as a parameter in the ASCAT sea ice extent algorithm. Image dilation and erosion techniques are employed to smooth the sea ice edge and correct misclassifications. ASCAT sea ice extent data is validated to overlapping OSCAT data.

Keywords: remote sensing, sea ice, OSCAT, ASCAT, cryosphere

ACKNOWLEDGMENTS

I would like to first and foremost thank Dr. Long for his many hours of instruction, assistance, correction, and patience. I especially appreciate his flexibility with my schedule while I worked part time during my schooling. I would also like to thank my committee who reviewed my research. Many thanks go to the members of the MERS Lab, past and present, who helped me along the way. A special acknowledgment goes to Sam Bury, who put extra hours in bringing our network back up after the Clyde building flooded. Finally, I would like to thank my wonderful wife, Heather, who has lovingly supported me through late nights and weekends working on this project.

TABLE OF CONTENTS

LIST OF FIGURES . . . . . **vi**

Chapter 1 Introduction **1**
1.1 Research Problem Statement 1
1.2 Thesis Statement 2
1.3 Research Contributions 3
1.4 Thesis Outline 4

Chapter 2 Background **5**
2.1 Active Microwave Remote Sensing 5
2.1.1 QuikSCAT 5
2.1.2 OSCAT 6
2.1.3 ASCAT 6
2.2 Passive Microwave Remote Sensing 7
2.2.1 SSM/I 8
2.3 Scatterometer Backscatter Measurements 9
2.4 RL-N Algorithm for Sea Ice Mapping 10
2.5 NASA Team Algorithm 12

Chapter 3 OSCAT sea ice algorithm **14**
3.1 Motivation 14
3.2 OSCAT Adjustments to the RL-N Algorithm 14
3.2.1 Reverse Processing Approach 16
3.3 Results 19
3.3.1 QuikSCAT Comparison 19
3.3.2 NASA Team Algorithm Comparison 21
3.4 Conclusion 24

Chapter 4 ASCAT sea ice algorithm **26**
4.1 ASCAT Azimuth Modulation 26
4.2 Normalized Difference Image 27
4.2.1 Likelihood Ratio Test 31
4.2.2 ASCAT Coverage Correction 32
4.3 ASCAT Sea Ice Mask Algorithm 33
4.4 Results 39
4.5 Conclusion 42

Chapter 5 Conclusion **43**
5.1 Contributions 43
5.1.1 OSCAT Algorithm Reverse Processing 43
5.1.2 OSCAT Sea Ice Extent Validation 43
5.1.3 ASCAT Normalized Difference Images 44

5.1.4 ASCAT Coverage Images 44
5.1.5 ASCAT Sea Ice Extent Validation 44
5.2 Future Work 44
5.2.1 Unified Scatterometer Sea Ice Extent Algorithm 45
5.2.2 OSCAT Sea Ice Extent Algorithm for OSCAT-2 45
5.2.3 Digital Image Processing Verification 45

REFERENCES **47**

Appendix A QuikSCAT Post Wind Mission Sea Ice Detection **50**
A.1 Introduction 50
A.2 Post Wind Mission 50
A.3 Data Averaging 51
A.4 Sea Ice Edge Classification Using QuikSCAT PWM Data 53
A.5 Conclusion 54

LIST OF FIGURES

2.1 OSCAT and QuikSCAT scanning geometry [1]. 7
2.2 ASCAT swath coverage [2]. 8
2.3 Contour plots of B_v versus γ distributions. The straight line and ellipse in both images represent the linear and Mahalanobis discriminant boundaries respectively [3]. 12

3.1 Images from the sea ice mask processing stages for day 163 of 2011. The left image is the h-pol σ^0 at 46° incidence angle used as one of the 4-D feature vector parameters applied to the image. The middle image is the final trinary sea ice mask. The right image is the final processed σ^0 sea ice mask. 15
3.2 Images from the sea ice mask processing stages for day 163 of 2010 illustrating the processing of images with missing data. Like in Fig. 3.1, the left image is the h-pol σ^0 at 46° incidence angle used as one of the 4-D feature vector parameters applied to the image. The middle image is the final trinary sea ice mask. The right image is the final processed σ^0 sea ice mask. 15
3.3 A sample of OSCAT SIR ice-masked images. Each of the four images has missing data due to data downlink problems. 17
3.4 Trinary OSCAT ice extent products corresponding to the four SIR images in Fig. 3.3. The trinary ice mask from the previous day is used to fill in the data gaps from the SIR images. 18
3.5 Comparison of forward and reverse processing techniques in total sea ice extent during days 274, 275, and 276 in 2010 in Antarctica, with QuikSCAT total sea ice extent data over the same days from 2007, 2008, and 2009. This sea ice extent data is processed after the long data gap in 2010. 20
3.6 Sea ice edge comparison in the Weddell Sea region of Antarctica showing the QuikSCAT ice edge (white line) and the OSCAT ice edge (black line). The background image is the OSCAT σ^0 image from day 319 of 2009. The South Shetland Islands and various icebergs, which are shown white in the ocean, are not included in the ice mask. 21
3.7 Sea ice extent over the lifetime of QuikSCAT (red) and OSCAT (green) in the (top) Antarctic and the (bottom) Arctic above 60° latitude. The data from the two instruments are compared to the SSM/I 0% and 30% sea ice extents. 22
3.8 Sea ice extent over the eighteen day overlap time period of QuikSCAT (red) and OSCAT (green) in the (top) Antarctic and the (bottom) Arctic above 60° latitude. The data from the two instruments are compared to the SSM/I 0% and 30% sea ice extents during that time period. 23
3.9 Sea ice extent differences with arbitrarily chosen SSM/I 0% data in the (top) Antarctic and the (bottom) Arctic. QuikSCAT, shown in red, concludes at the end of 2009. OSCAT, shown in green, begins right at the end of QuikSCAT and continues to the beginning of 2014. 24
3.10 Mean daily (top) Antarctic and (bottom) Arctic sea ice total extent from 2009 to 2014. The OSCAT extent is compared to SSM/I 0% and 30% mean sea ice extent. . 25

4.1 ASCAT sea ice and ocean histograms from the three antenna equation (left) and the two antenna equation (right). Data are taken from day 30 (top) and day 120 (bottom) of year 2013. 28
4.2 ASCAT sea ice and ocean histograms from the three antenna equation (left) and the two antenna equation (right). Data are taken from day 210 (top) and day 300 (bottom) of year 2013. 29
4.3 Receiver Operating Characteristic (ROC) curves generated from the histograms in Figs. 4.1 and 4.2. Regions of interest are highlighted in gray. 30
4.4 ASCAT coverage images for the aft and fore (left) and mid (right) antennas. Pixel values are the number of measurements over the time period of the SIR image. These images are from days 195 and 196 of 2013. 31
4.5 The four parameter images included in the ASCAT feature vector. Arctic images are taken from days 280 and 281 in 2012. Images are normalized difference (a), σ^0 standard deviation in dB (b), σ^0 in dB (c), and slope of σ^0 in dB/deg (d). 34
4.6 PPM for sea ice (left) and ocean (right) on day 195 of 2013. 35
4.7 ASCAT sea ice masks after initial Bayesian classification processing and various image processing steps. These images comes from ASCAT data from days 195 and 196 of 2013. 36
4.8 ASCAT sea ice masks before (a) and after (b) filling in empty pixels from lack of swath coverage. These images come from Antarctic ASCAT data from days 195 and 196 of 2013. 38
4.9 ASCAT Antarctic ice mask from day 224 of 2011 (right). The three antenna normalized difference image for that day is shown for comparison (left). 40
4.10 ASCAT Arctic ice mask from day 224 of 2011 (right). ASCAT V image (σ^0 standard deviation in dB) for that day is shown for comparison (left). 40
4.11 Sea ice extent comparison between ASCAT, OSCAT, and SSM/I data sets from 2010 to 2013 in the Antarctic. 41
4.12 Sea ice extent comparison between ASCAT, OSCAT, and SSM/I data sets from 2010 to 2013 in the Arctic. 42

A.1 QuikSCAT PWM SIR images of the Arctic from day 201 of 2010 (left) and day 51 of 2014 (right). The color scale is σ^0 in dB. The temporal difference shows the change in antenna position that happened in between these two dates. 51
A.2 QuikSCAT PWM SIR images of the Antarctic from day 201 of 2010 (left) and day 51 of 2014 (right). The color scale is σ^0 in dB. 52
A.3 QuikSCAT PWM SIR images of the Arctic averaged together from day 201 through day 210 of 2010 (left) and from day 50 through day 59 of 2014 (right). The color scale is σ^0 in dB. 53
A.4 QuikSCAT PWM SIR images of the Antarctic averaged together from day 201 through day 210 of 2010 (left) and from day 50 through day 59 of 2014 (right). The color scale is σ^0 in dB. 54
A.5 Comparison of QuikSCAT ice masks: normal QuikSCAT data on day 201 of year 2009 (left) and QuikSCAT PWM data from days 201 to 210 of 2010 (right). 55

CHAPTER 1. INTRODUCTION

Spaceborne wind scatterometers are primarily designed to measure wind speeds over the ocean. Scatterometers measure the normalized radar cross section (σ^0) of the Earth's surface [4]. This σ^0 backscatter measurement provides useful data for other scientific land and ice applications [5] [6]. One such application is the measurement of sea ice extent in the polar regions.

Sea ice in the polar regions moderates the global climate. Sea ice reflects sunlight very well and also insulates the Earth. Changes in sea ice extent therefore greatly affect temperatures in the polar regions. For this and other reasons, sea ice has been a key input in global climate models. Prior to remote sensing, sea ice was monitored using ships and buoys. This method only accurately measures sea ice data in very limited regions. Satellite remote sensing of sea ice extent gives a much broader area of coverage as well as daily measurements. This allows for tracking daily and yearly trends of sea ice growth and retreat.

Ku-band scatterometers are particularly well suited for mapping the sea ice extent because of the high contrast between σ^0 measurements of the ocean compared to sea ice. An algorithm has been developed to map the daily sea ice extent, in both the Arctic and Antarctic regions, from σ^0 measurements for the Ku-band NASA scatterometer (NSCAT) and for the Ku-band SeaWinds instrument aboard the Quick Scatterometer (QuikSCAT) [3].

1.1 Research Problem Statement

Sea ice properties have been measured by satellite microwave remote sensing instruments since 1972 when the Electrically Scanning Microwave Radiometer (ESMR) began measuring sea ice concentration [7]. Both passive and active instruments have been used independently or cooperatively to measure various sea ice conditions. Microwave passive radiometers measure sea ice extent by measuring the surface brightness temperature. The brightness temperature differences of sea ice and ocean allow for discrimination algorithms to distinguish between the two [8].

Active microwave scatterometers transmit a pulse and measure the returned radar backscatter (σ^0). Due to surface differences between sea ice and ocean, the σ^0 return between the two are generally different [9]. Often times, active and passive data are combined to increase reliability in sea ice extent algorithms [10].

Accurate sea ice maps are dependent on accurate and consistent data from all included instruments. While combining data from different instruments enhances the dependability of the sea ice extent measurements, it makes real time algorithms difficult. Thus it is valuable to develop algorithms for sea ice extent measurements using only one instrument. It is also valuable to maintain an independent scatterometer sea ice extent data set to validate against radiometer data sets. Both platforms bring pros and cons to sea ice detection, therefore it is valuable to have data from both.

Passive radiometers are valuable in sea ice measurements, however, they are often low resolution (25 km x 25 km). Active scatterometers have similar resolutions, but the Scatterometer Image Reconstruction (SIR) algorithm enhances scatterometer resolution. With the SIR algorithm, sea ice extent algorithms have been developed for stand-alone Ku-band instruments as mentioned previously [3, 10–12]. NSCAT and QuikSCAT consistently gathered daily σ^0 data for the duration of their respective missions. OSCAT started its mission days before QuikSCAT's conically scanning dish stopped turning making its sea ice extent algorithm no longer usable. OSCAT has very similar properties to QuikSCAT, however due to data drop outs throughout its mission, the sea ice extent algorithm designed for QuikSCAT could not be directly applied to OSCAT data.

The OSCAT mission ended in February 2014. Several scatterometers, including ASCAT, currently operate in C-band. Although C-band data does not discriminate between sea ice and ocean as well as Ku-band data, ASCAT provides polar scatterometer data beyond the completion of OSCAT's mission. Therefore a C-band sea ice extent data set would continue the scatterometer sea ice extent data set.

1.2 Thesis Statement

In order to continue the scatterometer sea ice extent data set, the algorithm designed for QuikSCAT is adapted and applied to OSCAT. Gaps in the OSCAT data set are accounted for. The OSCAT sea ice extent data set is compared and validated against passive radiometer sea ice extent data.

A Bayesian classification algorithm for measuring the sea ice extent using the C-band ASCAT is developed. Data from individual antennas on ASCAT are compared to better discriminate between sea ice and ocean. ASCAT sea ice extent data are compared to previous scatterometer data and passive radiometer data.

1.3 Research Contributions

The sea ice extent algorithm for QuikSCAT is applied to OSCAT data. The algorithm uses previous day masks to constrain sea ice growth and retreat in the processing of the current day mask. Due to this, sea ice masks are processed one day after another dependent on the previous day mask. Because long data gaps of up to 90 days persist in OSCAT data, previous day masks are not always available to constrain sea ice growth and retreat in the current day. In this case, following the forward time processing of the sea ice extent masks, a new backward time processing step is included to correct large data gaps.

The OSCAT sea ice extent data set overlaps the QuikSCAT sea ice extent data set by eighteen days before the QuikSCAT mission ends. These eighteen data points are compared to validate the OSCAT data set. Unfortunately, eighteen days is not a sufficient amount of time in a continuous yearly data set for validation. Therefore, the OSCAT sea ice extent data set is also compared to the passive microwave sensor, Special Sensor Microwave Imager (SSM/I) sea ice extent data set.

To further extend the scatterometer ice edge data set, a Bayesian classification algorithm for ASCAT sea ice extent mapping is refined from work done by Steven Reeves [13]. A normalized difference equation is developed to include contributions from the fore, mid, and aft antennas. The normalized difference equation better discriminates between sea ice and ocean. ASCAT coverage images are used to eliminate misclassifications around areas of low ASCAT data coverage. Image processing techniques are included to refine the sea ice extent edge.

The ASCAT sea ice extent data is validated to both the QuikSCAT and the OSCAT sea ice extent data set. This validation is particularly important because of the C-band to Ku-band comparison.

1.4 Thesis Outline

This thesis has the following outline. Chapter 2 discusses necessary background information about the discussed scatterometers, scatterometer image processing, and previous sea ice extent algorithms. Chapter 3 presents the adjustments applied to the QuikSCAT sea ice extent algorithm for use on OSCAT data. The ASCAT Bayesian sea ice classification algorithm is discussed in Chapter 4. Chapter 5 summarizes the results and concludes the thesis. An appendix explores automated QuikSCAT post wind mission data sea ice mapping.

CHAPTER 2. BACKGROUND

The following sections discuss the details of various active microwave remote sensors as well as a passive microwave sensors. Scatterometer backscatter measurements as well as image reconstruction techniques are also examined. The chapter is completed with information on sea ice extent algorithms previously developed.

2.1 Active Microwave Remote Sensing

Active microwave remote sensors are active because they both transmit and receive microwave pulses. Scatterometers are a type of active sensor that measure the radar backscatter of the Earth's surface. Reconstruction techniques create enhanced resolution images of the surface from the backscatter, or σ^0, measurements [5]. High resolution images are developed by taking advantage of Doppler filters and/or range gating [9]. The following sections describe the different scatterometers discussed in this thesis.

2.1.1 QuikSCAT

The SeaWinds instrument on the QuikSCAT satellite (QuikSCAT) is a conically scanning dual pencil-beam scatterometer. QuikSCAT was launched in 1999 and was intended as a "quick recovery" mission following the end of the NASA Scatterometer (NSCAT) mission. The satellite was placed in an 803 km altitude, sun-synchronous orbit [14]. The mission was intended to only last two years, but because of its consistent data collection, the SeaWinds mission lasted until 2009, ten years after it was launched.

QuikSCAT calculates a wind vector based on σ^0 values on the surface at multiple azimuth angles. Unlike previous wind scatterometers that had typical fan beam geometries, QuikSCAT has a rotating pencil-beam design which allows for many azimuth angle measurements at a fixed incidence angle. This improves surface coverage as well as providing the multiple azimuth angles

required for wind retrieval [4]. Backscatter data are retrieved as 'slices' and 'eggs.' Slices are 4-6 km long by 20 km wide. Eggs are formed by summing slices into a larger 20 km by 30 km area [15].

Scatterometers were originally designed to simply measure wind speeds over the ocean; however, scientists found that scatterometer data provides useful information in land and ice applications [5]. Scatterometers are impervious to cloud cover or lack of sunlight making them especially useful in polar regions where it is often overcast and dark through much of the polar winters. Early Ku-band instruments, such as NSCAT, were found useful in measuring polar ice extent and classifying sea ice types. Algorithms were developed to utilize σ^0 measurements over ocean and sea ice surfaces. Because of QuikSCAT's surface coverage and consistent daily data, algorithms, to be discussed later, were developed to measure sea ice extent using QuikSCAT data.

2.1.2 OSCAT

OSCAT is another conically scanning dual pencil-beam scatterometer designed and built by the India Space Research Organization (ISRO). It was launched on Oceansat-2 on September 23, 2009. Similar to SeaWinds, OSCAT uses a one meter dish antenna rotating at twenty rpm. The dish illuminates two "spot" beams of about 25 km x 55 km area on the ground as shown in Fig. 2.1. The outer beam is vertically polarized at 49 degrees incidence angle and the inner beam is horizontally polarized at 43 degrees incidence angle. It operates at 13.515 GHz (Ku-band) [16]. Oceansat-2 flies in a sun-synchronous orbit providing OSCAT with full global coverage. It also covers 90% of the ocean surface in 24 hours with its rotating dish geometry [16]. OSCAT data, like QuikSCAT, is measured in both slice and egg data.

2.1.3 ASCAT

The first Advanced Scatterometer (ASCAT) was launched by the European Space Agency (ESA) on board the Meteorological Operational (MetOp)-A satellite in October 2006. ASCAT is operated by the EUropean organisation for the exploitation of METeorological SATellites (EUMETSAT) [17]. Data were first collected in May 2007. ASCAT is a 5.255 GHz (C-band) fan-beam scatterometer with two sets of three vertically polarized antennas. The three antennas point at 45,

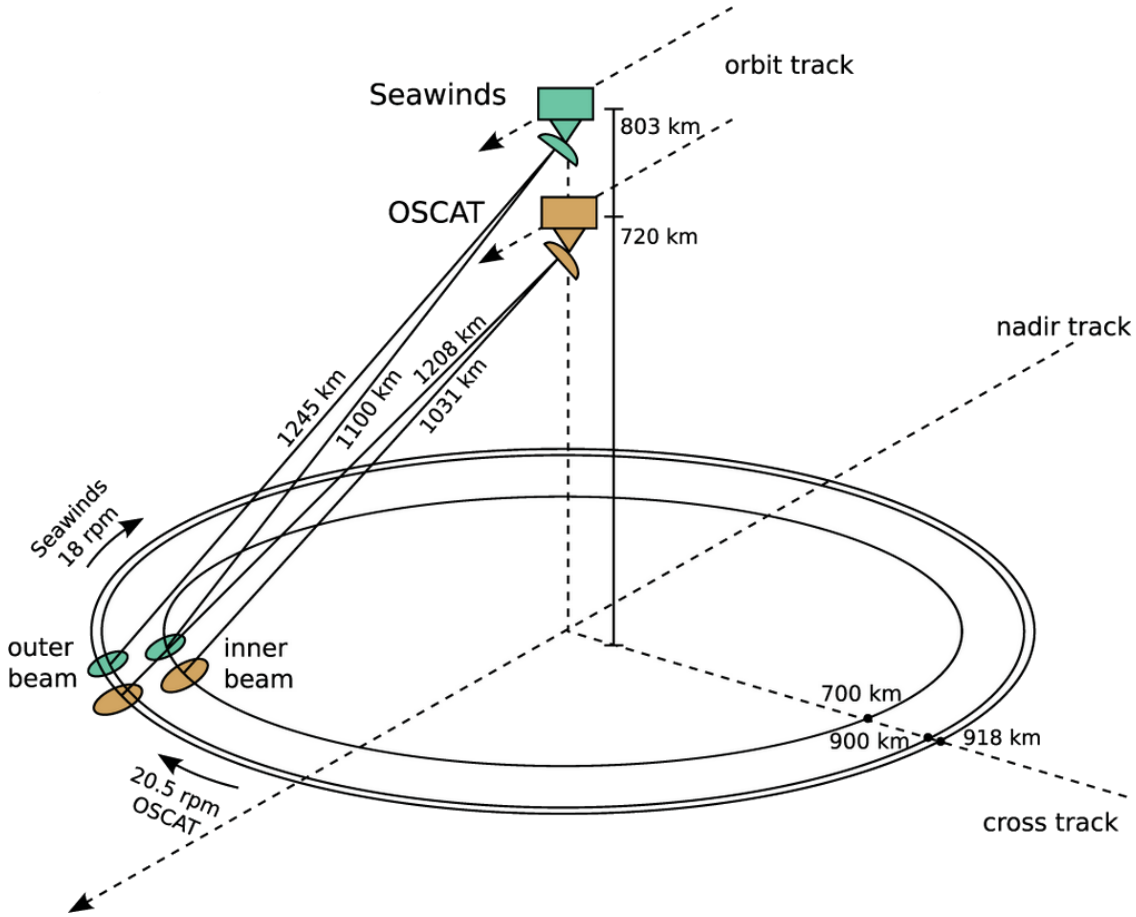

Figure 2.1: OSCAT and QuikSCAT scanning geometry [1].

90, and 135 degrees relative to the satellite track. The two sets of antennas are on either side of the instrument. These beams illuminate 550 km-wide swaths on both sides of the flight track with a nadir gap of about 700 km [17]. This coverage is shown in Fig. 2.2. Because of the limited swath coverage, ASCAT does not achieve full daily polar coverage like QuikSCAT and OSCAT. This is adjusted for in the ASCAT sea ice extent algorithm.

2.2 Passive Microwave Remote Sensing

Passive sensors do not transmit microwave pulses like active sensors. Instead they only have a receive antenna that measures low levels of microwave radiation [9]. This radiation is emitted from all matter due to atomic movement and material properties. Radiometers, passive microwave instruments, are used to measure the brightness temperature of the Earth's surface.

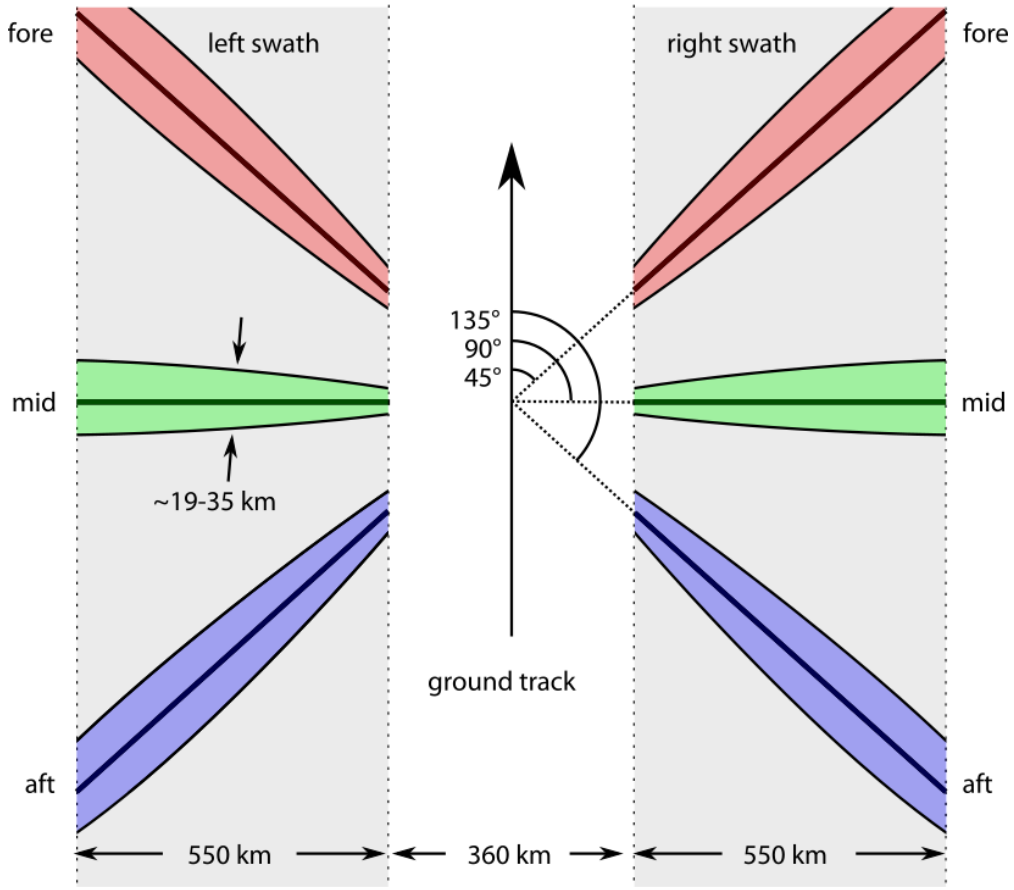

Figure 2.2: ASCAT swath coverage [2].

Data from several radiometers have been used to determine the sea ice extent and classify sea ice type in the polar regions because of the difference in brightness temperature between sea ice and ocean. The following radiometer is involved in this study [18–20].

2.2.1 SSM/I

The Special Sensor Microwave/Imager (SSM/I) was launched in June, 1987 on board the Defense Meteorological Satellite Program (DMSP) F8 satellite. With a sun-synchronous polar orbit, SSM/I is well suited for polar ice studies. The instrument is linearly polarized with seven channels operating at microwave frequencies of 19.36, 22.235, 37.0, and 85.5 GHz. The 85.5 GHz frequency resolution is 15x13 km and the 19.35 GHz resolution is 69x43 km [21].

The seven channels are fed by a corrugated, broad-band horn antenna reflected by an offset parabolic reflector. The system rotates continuously at 31.6 rpm and covers a swath width of about 1400 km. The incidence angle of the antenna beam with the Earth's surface is 53.1 degrees.

Data from radiometers have been used in sea ice observations since 1972. It started with the Electrically Scanning Microwave Radiometer (ESMR) [7] and later the Scanning Multichannel Microwave Radiometer (SMMR) [22]. SSM/I has contributed to sea ice observations since 1987 [23]. The data is processed using the NASA Team sea ice algorithm to determine ice concentrations in the polar regions. The NASA Team sea ice algorithm is discussed later in this chapter.

2.3 Scatterometer Backscatter Measurements

Scatterometers measure the normalized radar backscatter coefficient (σ^0) of the Earth's surface. The σ^0 measurement is derived from the radar equation,

$$\sigma^0 = \frac{(4\pi)^3 R^4 L}{P_t G^2 \lambda^2 A} P_S, \tag{2.1}$$

where R is the slant range to the surface, P_t is the transmitted power, P_S is the received backscattered power, L represents known system losses, G is antenna gain, A is the effective illuminated area, and λ is the wavelength of the transmitted radiation [9]. The σ^0 measurements are taken over a range of incidence angles. A linear function of the measurement incidence angle

$$10\log_{10}\sigma^0(\theta) = A + B(\theta - 40^\circ), \tag{2.2}$$

where θ is the incidence angle of the observation, models σ^0 measurements. A and B are functions of the observed surface characteristics. A is the σ^0 value at 40° incidence angle, and B is the dependence of σ^0 on incidence angle.

Scatterometers were not originally designed for imaging, but by combining multiple passes, high resolution images of A and B can be created to support studies of the Earth's surface. The Scatterometer Image Reconstruction with Filter (SIRF) algorithm produces A and B images for several scatterometers including OSCAT and ASCAT [24] [25]. The SIRF algorithm enhances effective scatterometer image resolution by combining σ^0 measurements from multiple passes.

These resolution-enhanced images are used in algorithms for sea ice mapping where they provide higher spatial resolution ice masks than corresponding masks from passive sensors [3] [11] [10].

2.4 RL-N Algorithm for Sea Ice Mapping

The NSCAT algorithm for sea ice mapping [3] was developed by Remund and Long (RL-N) and later adapted for QuikSCAT [26]. It uses an iterative maximum-likelihood classifier with fixed thresholds to classify sea ice pixels from QuikSCAT Scatterometer Image Reconstruction (SIR) images derived from the σ^0 measurements [25]. For each daily image pixel, four parameters are combined into a 4-D feature vector. The parameters are chosen because they demonstrate sufficient difference between sea ice pixel values and ocean pixel values. This allows the algorithm to discriminate between sea ice and ocean with low error. These parameters are (1) a modified copolarization (copol) ratio, (2) the h-pol σ^0, and the standard deviations of (3) v-pol and (4) h-pol σ^0 estimate error. The modified copol ratio (γ_{sw}) is the ratio of the v-pol A image at 54° incidence and the h-pol A image at 46° incidence. This is the difference in log space of v-pol and h-pol σ^0. The ratio in general is lower with sea ice volume scattering as compared to ocean surface scattering. The h-pol σ^0 image (A_h^{46}) is the h-pol A image at 46° incidence. H-pol and v-pol σ^0 measurements are typically similar over sea ice, but h-pol measurements over the ocean tend to be much lower than v-pol measurements making h-pol A images more desirable as a parameter. The σ^0 estimate error standard deviations for both v-pol (κ_v) and h-pol (κ_h) are included because azimuthal modulation over wind-roughened ocean surfaces results in large standard deviations whereas sea ice has been shown to have minimal azimuthal dependence and therefore low error standard deviation.

The parameters are concatenated into a 4-D hyperspace of measurement vectors

$$\vec{x} = [\gamma_{sw}\ A_h^{46}\ \kappa_v\ \kappa_h]^T. \tag{2.3}$$

After collection, each feature vector is normalized to a mean of zero and a variance of one. Remund and Long [26] found that sea ice detection performance is better when the copol ratio is weighted in importance four times more than the other three parameters when generating the histogram. A daily 4-D histogram is computed to estimate a bimodal sea ice/ocean joint distribution for that day.

A linear discrimination technique is first applied for classification. An automated 4-D histogram search algorithm locates the saddle point on the transect connecting the ocean and sea ice peaks. A line orthogonal to the transect is drawn through the saddle point and the pixels are then classified as ocean or sea ice based on which side of the line they fall on as shown in Fig. 2.3.

This initial classification is improved with an iterative Maximum Likelihood (ML) classification technique adopted from [12]. The two modes in the 4-D histogram are assumed to be Gaussian. This assumption is used in the RL-N algorithm for efficiency in near real-time use. The algorithm performance is improved when derived histograms approximate the distribution [11], but the Gaussian assumption is more efficient since the distribution can be parameterized by means and variances. With the Gaussian assumption, the ML algorithm minimizes the "ML distance metric"

$$C_{ML} = argmin_c[\log|K_c| + (\vec{y} - \vec{\mu}_c)^T K_c^{-1}(\vec{y} - \vec{\mu}_c)], \tag{2.4}$$

where $\vec{y}$ is the standardized and weighted data vector, $\vec{\mu}_c$ is the mean vector for either sea ice or ocean defined by C, and K_c is the covariance matrix for sea ice or ocean. The mean vectors and covariance matrices are estimated from the linear discrimination step for the first iteration. After the first iteration, new statistics are computed and a second iteration of the ML algorithm is applied.

Misclassifications still occur because high winds over the ocean at times causes σ^0 measurements over the ocean to look like sea ice σ^0 values. Also, melting ice σ^0 measurements can look like ocean. A region growing technique [3] is applied to eliminate these misclassifications. The technique selects a known area of sea ice in the image. Pixels classified as sea ice directly adjacent to this known area are included in the sea ice region. This region "grows" until the edge is detected. All pixels inside the sea ice edge are classified as sea ice and all pixels outside this edge are classified as ocean. This results in ice-free polynyas inside the sea ice edge being classified as sea ice. Since the purpose is to generate a sea ice extent, this misclassification is acceptable.

The remaining algorithm flaws occur on the sea ice edge in the form of misclassified "extrusions" or "indentations" that persist following the classification procedure and region growing process. The final step of the algorithm is sea ice growth/retreat constraint filtering to curb these misclassifications. Image dilation and erosion techniques [27, 28] combine the previous day's sea ice extent σ^0 backscatter image with a threshold of 200-km maximum edge motion per day [26].

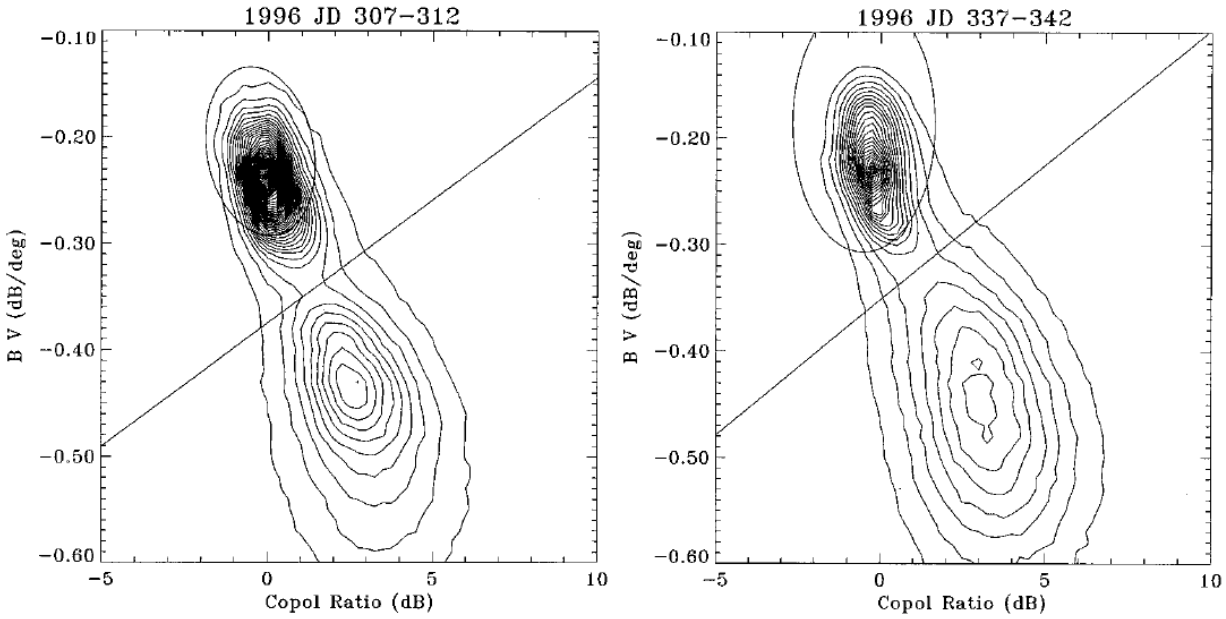

Figure 2.3: Contour plots of B_v versus γ distributions. The straight line and ellipse in both images represent the linear and Mahalanobis discriminant boundaries respectively [3].

Following erosion, disconnected extrusions on the ice edge are reclassified as water; following dilation, filled indentations are reclassified as ice. The result is a trinary mask with different values assigned to water, ice, and land. Example images from the algorithm applied to OSCAT are displayed in Fig. 3.4.

2.5 NASA Team Algorithm

The NASA Team algorithm uses radiometer data to determine a percentage of ice concentration for each pixel in the polar regions. It uses brightness temperature measurements to determine ratios used for classification. The two ratios used are the polarization ratio

$$PR(v) = \frac{TB(vV) - TB(vH)}{TB(vV) + TB(vH)} \tag{2.5}$$

and the spectral gradient ratio

$$GR(v_1 p v_2 p) = \frac{TB(v_1 p) - TB(v_2 p)}{TB(v_1 p) + TB(v_2 p)}, \tag{2.6}$$

where TB is the brightness temperature, ν is the frequency and p is the polarized component (vertical V or horizontal H). A value is determined for both that defines a 100% ice concentration. Another point is defined as open water. Each pixel is then assigned a percentage ice concentration based on the distance of its polarization ratio and spectral gradient ratio value from the open water point and sea ice point [29].

CHAPTER 3. OSCAT SEA ICE ALGORITHM

3.1 Motivation

In order to continue the scatterometer sea ice extent data set, the RL-N algorithm for QuikSCAT sea ice mapping [1] is adapted and applied to OSCAT. The QuikSCAT wind mission ended in 2009, but continuation of the Ku-band scatterometer data climate record is made possible through the operation of OSCAT, which began its data collection eighteen days before the end of QuikSCAT's wind mission. OSCAT operates with the same pencil-beam design as QuikSCAT. The similarity enables the QuikSCAT sea ice extent algorithm to be applied to OSCAT data. However data gaps persist in the OSCAT data set. To address this problem, the OSCAT sea ice extent algorithm is modified from the QuikSCAT algorithm to account for the gaps in the OSCAT data set [30]. This chapter discusses these adjustments and validates the OSCAT ice extent data set with QuikSCAT and Special Sensor Microwave/Imager (SSM/I) data sets.

3.2 OSCAT Adjustments to the RL-N Algorithm

Daily OSCAT SIR images are processed into sea ice maps using the modified QuikSCAT ice mapping algorithm. Available data for OSCAT, obtained as L1B OSCAT V1.1 data processed by the Indian Space Research Organization (ISRO) and obtained from the European Organisation for the Exploitation of Meteorological Satellites (EUMETSAT) via the National Oceanic and Atmospheric Administration (NOAA), ranges from day 309 of year 2009 to day 51 in year 2014. OSCAT had known mounting and latitude dependent bias. However, in the polar regions the variation of the bias with location is relatively small and thus ignored in the ice mapping processing. Since the water/ice threshold is set dynamically, the small mean bias has no impact on the algorithm performance or the resulting ice masks. Most days are processed normally as shown in Fig. 3.1. The various parameters, such as the h-pol σ^0 backscatter image shown on the left, are run

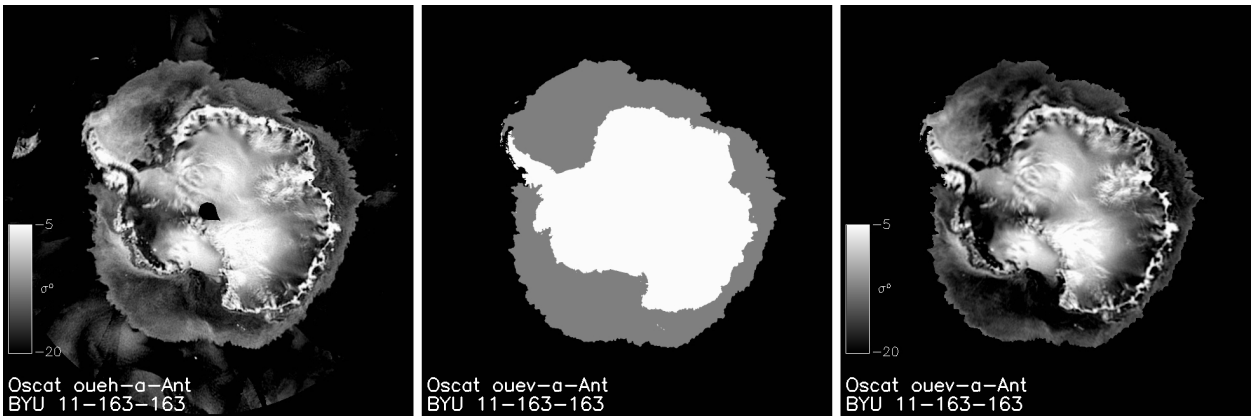

Figure 3.1: Images from the sea ice mask processing stages for day 163 of 2011. The left image is the h-pol σ^0 at 46° incidence angle used as one of the 4-D feature vector parameters applied to the image. The middle image is the final trinary sea ice mask. The right image is the final processed σ^0 sea ice mask.

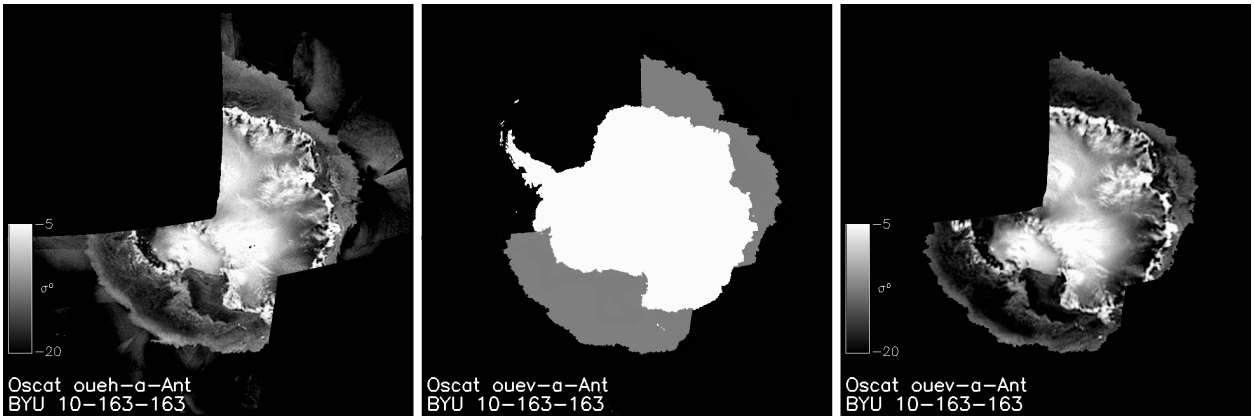

Figure 3.2: Images from the sea ice mask processing stages for day 163 of 2010 illustrating the processing of images with missing data. Like in Fig. 3.1, the left image is the h-pol σ^0 at 46° incidence angle used as one of the 4-D feature vector parameters applied to the image. The middle image is the final trinary sea ice mask. The right image is the final processed σ^0 sea ice mask.

through the algorithm after being normalized to a mean of zero and a variance of one. The resulting masked σ^0 backscatter image is shown on the right. Due to data dropouts, however, missing data is prevalent in a number of days during OSCAT's mission. This is illustrated in Fig. 3.2. The algorithm classifies the data available as shown in the middle and right images of Fig. 3.2, but portions corresponding to missing data remain blank. The consequence of this missing data arises when using this sea ice extent image to constrain allowable sea ice movement for the next day.

The QuikSCAT sea ice mask algorithm uses the σ^0 backscatter ice mask as the previous day's constraint mask. This works exceptionally well with QuikSCAT because the data is continuous. Modifications are applied to the OSCAT sea ice extent algorithm to overcome the coverage inconsistency in data for OSCAT. Fig. 3.3 shows a sample of OSCAT σ^0 ice mask images with missing data from four different days of OSCAT's mission, including the finished SIR ice mask sample of day 163 from 2010. The missing data limits the utility of these σ^0 backscatter sea ice masks for use as the previous day constraint for the following day's mask.

To compensate for this issue, the missing data for the trinary mask is filled in with the previous day's trinary mask. The data gaps shown in Fig. 3.3 are filled in using data from the trinary ice masks of the previous day as shown in Fig. 3.4. With this correction, OSCAT sea ice extent images are processed using the trinary image as the previous day's constraint rather than the σ^0 backscatter sea ice extent image, which is used for the QuikSCAT algorithm. By doing so, sea ice extent maps from days with partially missing data are filled in properly with correct data and the resulting OSCAT sea ice extent data set is more consistent.

3.2.1 Reverse Processing Approach

This simple procedure does not, however, correct all sea ice extent problems that arise from consecutive days of missing data in the OSCAT data set. One such stretch of days for OSCAT occurs from day 182 to day 273 in 2010. Due to power fluctuations [31], σ^0 data during that time is incorrect and therefore images over this period are not processed. The lack of data causes a problem when attempting to process the sea ice extent map for day 274. The nearest sea ice extent map available for use as the previous day constraint mask comes from day 181. Using day 181 as the constraint mask for day 274 would inaccurately constrain the sea ice growth for day 274.

To address this problem, a reverse time processing approach is used when long gaps occur. Rather than using the previous day as the constraint mask, the current day is used as the constraint mask for the previous day. With this approach, the trinary mask for day 278 of 2010 is used as the constraint for day 277 while day 277 is reprocessed. The new trinary mask from day 277 is then used as the constraint for day 276 and so on until day 274 is reprocessed with a more accurate constraint mask based on the future.

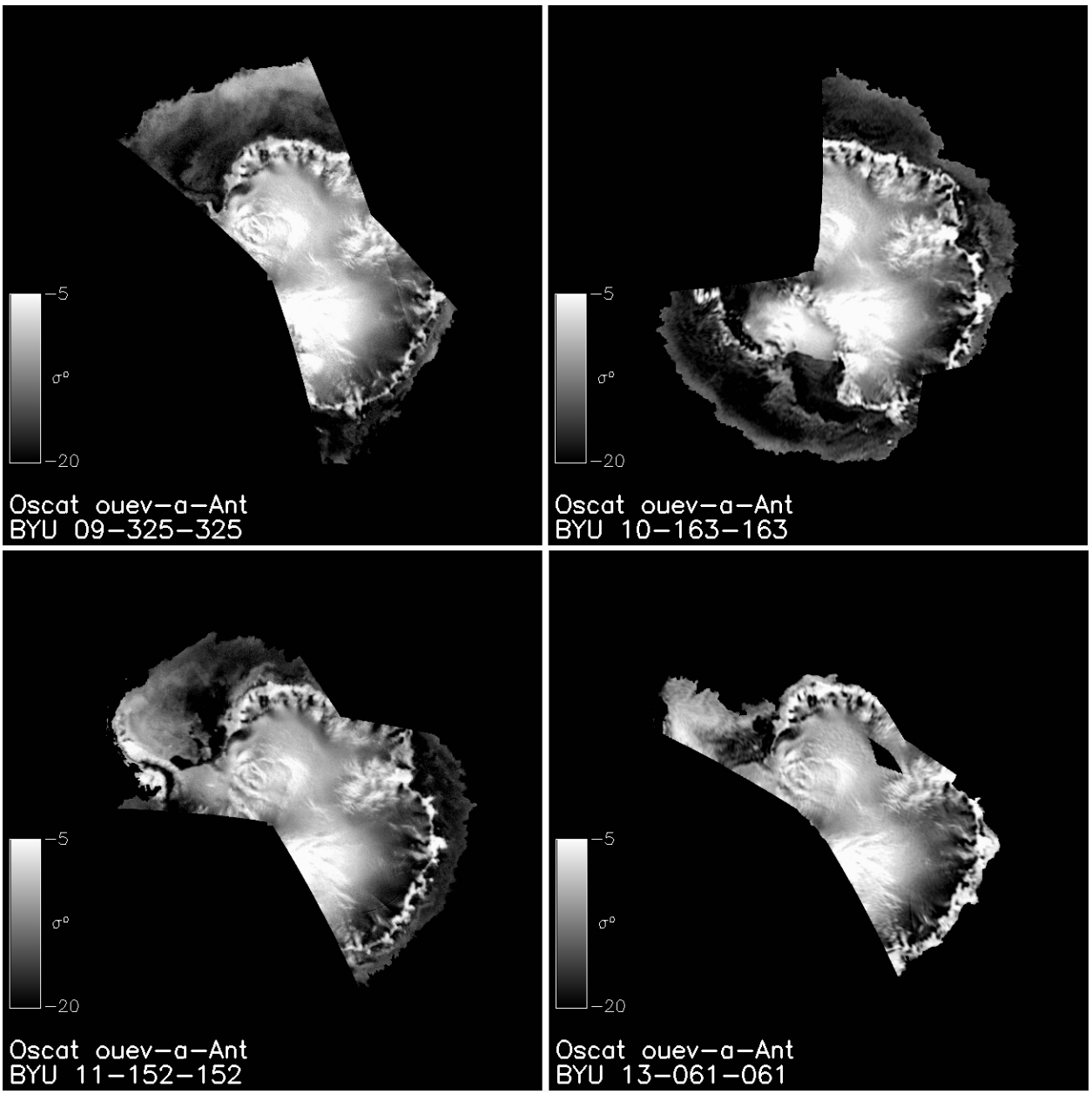

Figure 3.3: A sample of OSCAT SIR ice-masked images. Each of the four images has missing data due to data downlink problems.

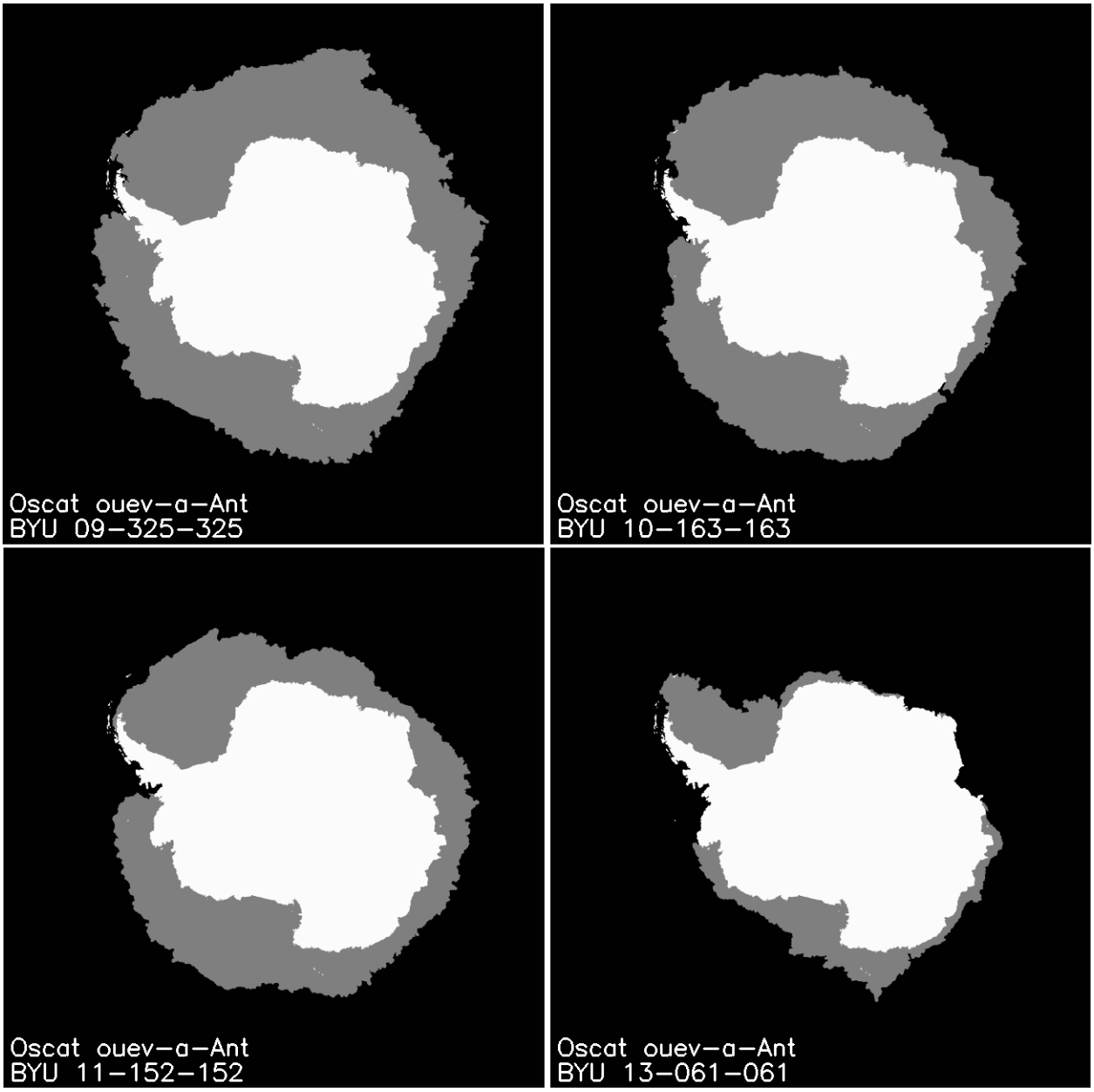

Figure 3.4: Trinary OSCAT ice extent products corresponding to the four SIR images in Fig. 3.3. The trinary ice mask from the previous day is used to fill in the data gaps from the SIR images.

The reprocessed sea ice mask of day 274 is a much better representation of the actual sea ice extent compared to the first processed mask as shown in Fig. 3.5. The results of the forward processing technique is represented by the dot-dashed line, and the reverse processing technique is represented by the dashed line. For comparison, the previous three years of QuikSCAT sea ice extent data for these days are represented by the solid lines. The reverse processing technique follows the ice extent trends of previous years better than the forward processing technique. The forward processing technique requires two to three days to catch up. This supports the use of the reverse processing technique following large gaps in the data.

Fortunately, the data gap in 2010 is the only gap longer than fifteen days. There is another data gap of fifteen days in 2012. All other data gaps are five days or less. Because these data gaps happen randomly throughout the data set and the gaps make up only 10% of the potential OSCAT data set, OSCAT yearly trends and means are not negatively affected by these data gaps. The noncausal reverse processing approach is used to correct for data gaps of two days or more.

3.3 Results

The modified sea ice extent algorithm is applied to the entire OSCAT mission. Coupled with the QuikSCAT data set, this provides a nearly continuous sea ice extent data set for the polar regions from 1999 to 2014. The OSCAT sea ice extent is validated using the overlapping period with QuikSCAT and the NASA Team algorithm applied to SSM/I.

3.3.1 QuikSCAT Comparison

QuikSCAT and OSCAT overlap from day 309 to day 327 in 2009. Due to three days of missing OSCAT data during this span, there are sixteen days of data that overlap between the instruments. The two data sets are compared during this overlap period. Fig. 3.6 shows a QuikSCAT slice SIR image of the Weddell Sea from day 319 of 2009. The derived ice edges from QuikSCAT and OSCAT are superimposed on the QuikSCAT SIR image from 2009. Note the close correlation between the ice masks of the two sensors. Note also the icebergs at the top of the image, which are correctly removed from the overall sea ice extent. The Antarctic Peninsula and the South Shetland Islands, prominently displayed in Fig. 3.6, are masked out of the algorithm

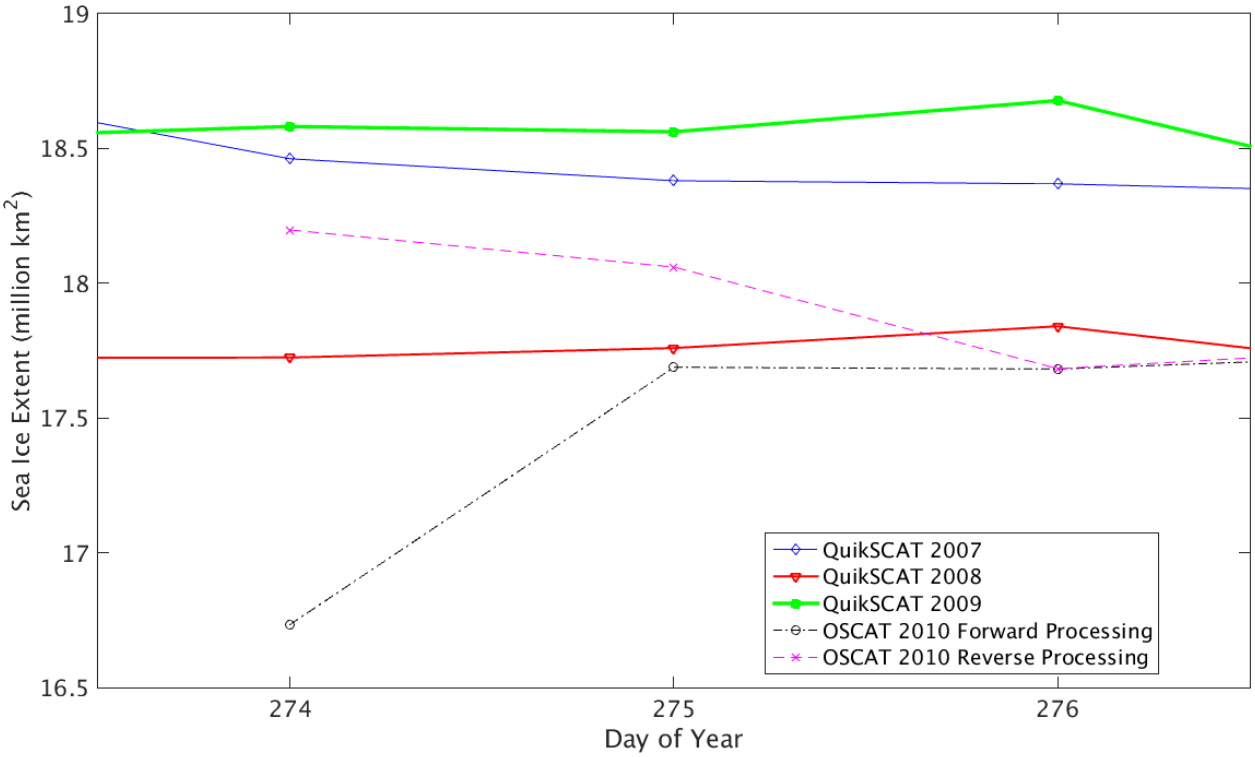

Figure 3.5: Comparison of forward and reverse processing techniques in total sea ice extent during days 274, 275, and 276 in 2010 in Antarctica, with QuikSCAT total sea ice extent data over the same days from 2007, 2008, and 2009. This sea ice extent data is processed after the long data gap in 2010.

processing and are therefore not included in the sea ice extent. It may be that the darker splotches along the lower coast of the Antarctic Peninsula are polynyas, areas of open water surrounded by ice. While these are technically not areas of sea ice, they are included in the sea ice extent as being inside the larger boundary between sea ice and ocean.

The root-mean-square error (RMSE) between the sea ice extents measured by the two instruments over the sixteen overlapping days is 0.12 million km^2 for the Antarctic region and 0.24 million km^2 for the Arctic region. From the QuikSCAT and OSCAT comparisons, we conclude that the OSCAT modified sea ice extent algorithm reasonably matches the QuikSCAT ice extent data set during the overlapping period in both the Arctic and Antarctic regions.

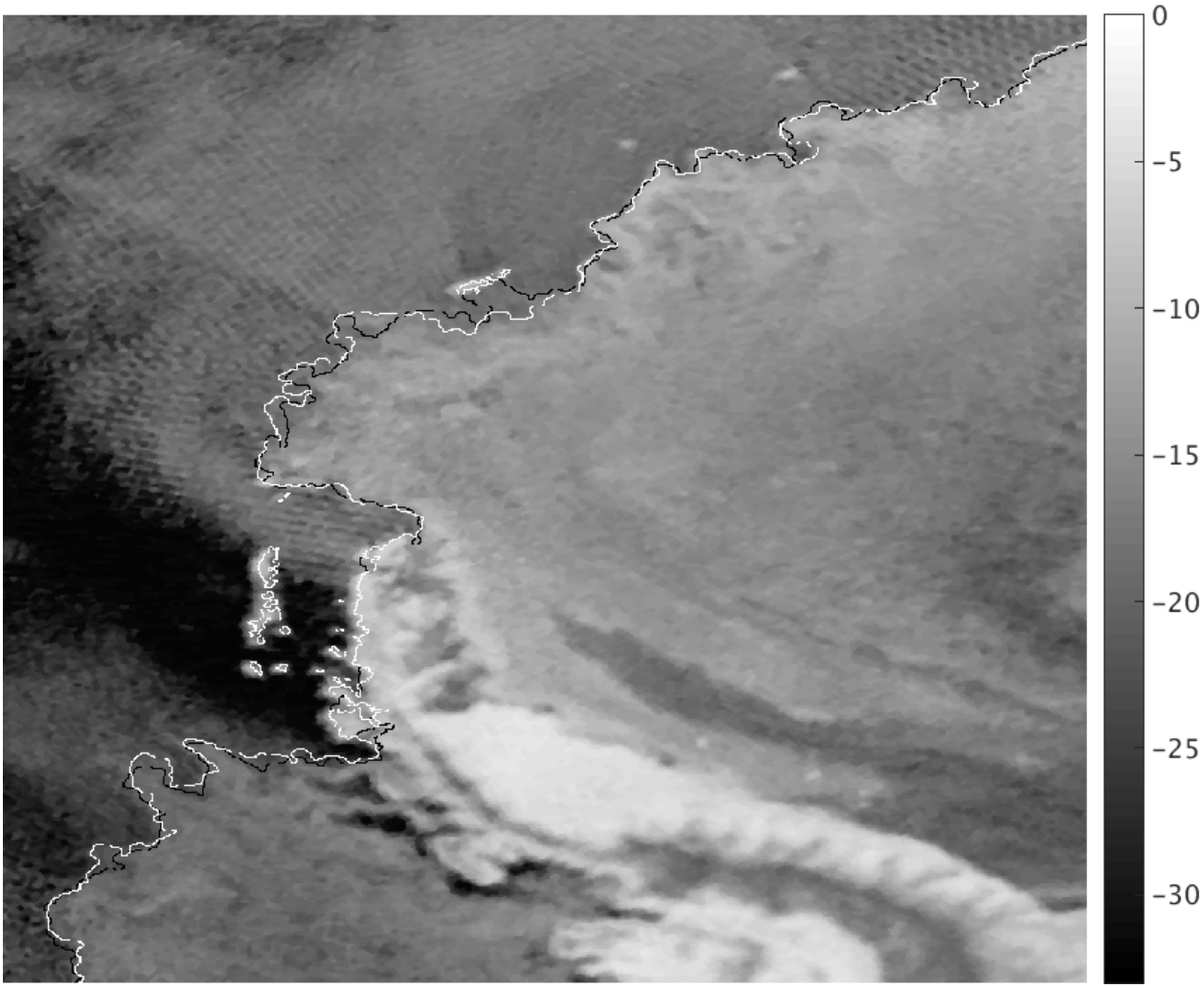

Figure 3.6: Sea ice edge comparison in the Weddell Sea region of Antarctica showing the QuikSCAT ice edge (white line) and the OSCAT ice edge (black line). The background image is the OSCAT σ^0 image from day 319 of 2009. The South Shetland Islands and various icebergs, which are shown white in the ocean, are not included in the ice mask.

3.3.2 NASA Team Algorithm Comparison

The OSCAT data set daily measurements of total sea ice area are compared to SSM/I sea ice extent data. SSM/I sea ice classification is from the NASA Team algorithm [32]. This algorithm classifies ice based on multifrequency dual-polarization data from the passive radiometer, Special Sensor Microwave Imager (SSM/I). This data is retrieved from the National Snow and Ice Data Center (NSIDC) [33].

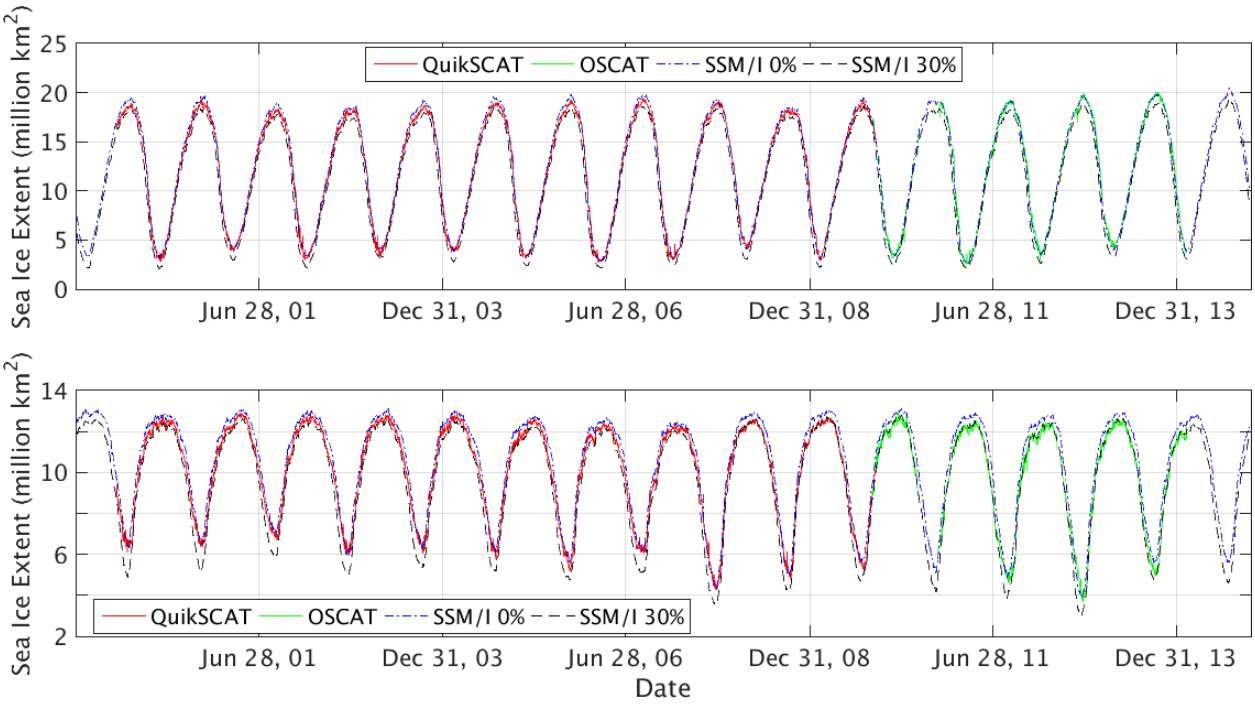

Figure 3.7: Sea ice extent over the lifetime of QuikSCAT (red) and OSCAT (green) in the (top) Antarctic and the (bottom) Arctic above 60° latitude. The data from the two instruments are compared to the SSM/I 0% and 30% sea ice extents.

OSCAT pixels flagged as ice are summed for each day and a total area is computed using the 4.5-km pixel size of the polar stereographic projection. SSM/I-generated sea ice extent map pixels are on a 25-km polar stereographic projection grid. The NASA Team algorithm produces various percent ice concentrations that are used for comparison. Total sea ice extent for different concentrations is calculated by summing only pixels above the concentration threshold.

The OSCAT daily sea ice extent results for the two polar regions from 2009 to 2014 are shown in Fig. 3.7. The QuikSCAT daily sea ice extent results for its mission life from 1999 to 2009 are included to create a continuous time-series of data. The SSM/I-measured 0% and 30% ice concentration extent values are given for comparison. The OSCAT- and QuikSCAT-measured sea ice extents in the Arctic are calculated only from sea ice above 60° latitude to align with SSM/I sea ice extent data. Despite some inconsistency in OSCAT data, it is seen in Fig. 3.7 that OSCAT-measured sea ice extent generally falls between the SSM/I 0% and 30% measured sea ice extent, which is consistent with QuikSCAT performance [26]. The comparison between OSCAT and QuikSCAT algorithms during the eighteen day overlap period are closely compared in Fig. 3.8.

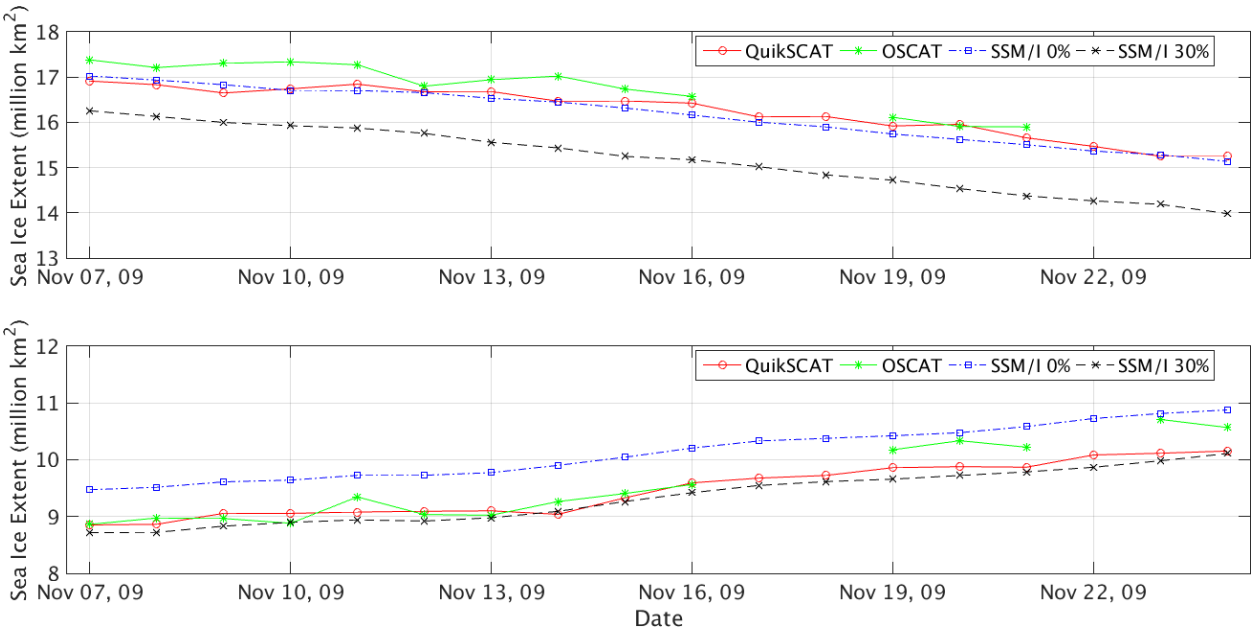

Figure 3.8: Sea ice extent over the eighteen day overlap time period of QuikSCAT (red) and OSCAT (green) in the (top) Antarctic and the (bottom) Arctic above 60° latitude. The data from the two instruments are compared to the SSM/I 0% and 30% sea ice extents during that time period.

There are data points missing from the OSCAT data set during these eighteen days where there are days of missing data or a very small part of data available. In general, OSCAT data gives slightly larger sea ice extent measurements than QuikSCAT data. This could be a result of differences in resolution and coverage between the two instruments during this time period.

Sea ice extent differences between the different instruments are displayed in Fig. 3.9. The OSCAT data shows similar trends to QuikSCAT data. Daily means of the sea ice extent of both the Antarctic and Arctic regions over the life of OSCAT are shown in Fig. 3.10. Both are shown in comparison to SSM/I 0% and 30% daily mean sea ice extents. The Antarctic extent in particular shows that the OSCAT sea ice extent correlates to the SSM/I 0% ice concentration during the austral summer and to the SSM/I 30% ice concentration during the austral winter. The differences may be caused by different frequency use, passive versus active microwave measurements, different polarizations, algorithm methods, etc. A deeper explanation of these differences is found in [26, 34].

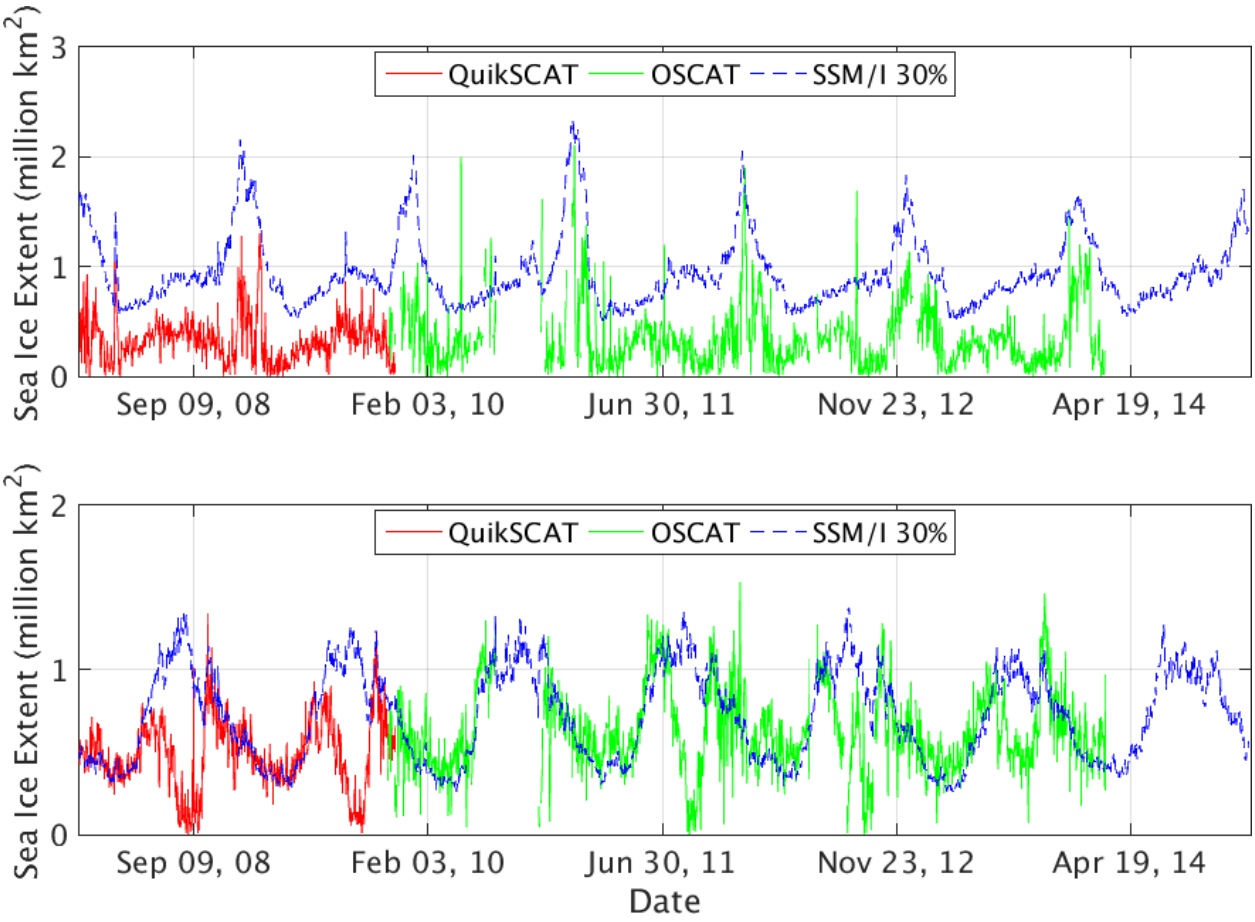

Figure 3.9: Sea ice extent differences with arbitrarily chosen SSM/I 0% data in the (top) Antarctic and the (bottom) Arctic. QuikSCAT, shown in red, concludes at the end of 2009. OSCAT, shown in green, begins right at the end of QuikSCAT and continues to the beginning of 2014.

3.4 Conclusion

The QuikSCAT ice edge algorithm has proven useful for the QuikSCAT data set [26]. Non-causal processing of OSCAT data using that algorithm creates an ice extent data set that continues where QuikSCAT left off. The OSCAT data set is validated using the SSM/I-derived NASA Team algorithm 0%-30% ice extents.

The QuikSCAT and OSCAT data sets are combined to provide a continuous data set of Ku-band scatterometer-derived sea ice extents from 1999 to 2014. This data set is publicly available from the Scatterometer Climate Record Pathfinder (SCP) (www.scp.byu.edu).

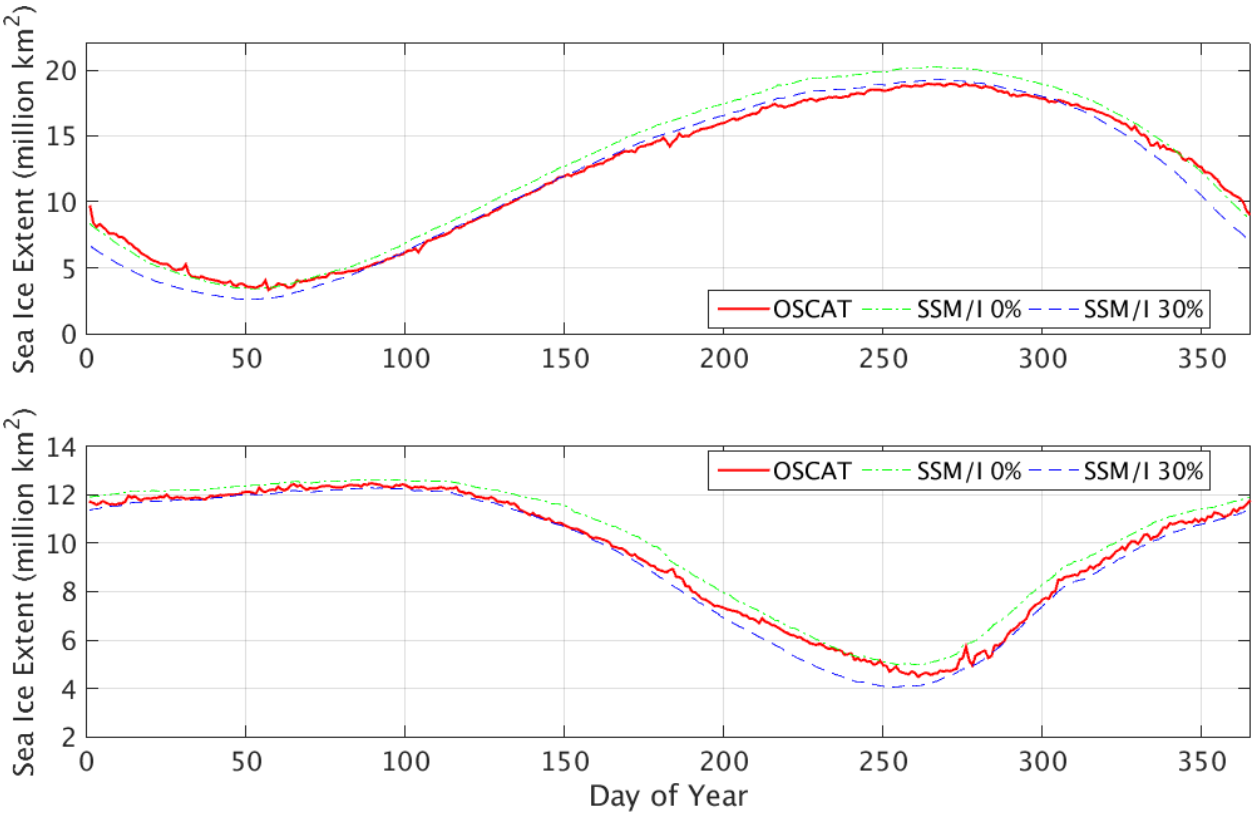

Figure 3.10: Mean daily (top) Antarctic and (bottom) Arctic sea ice total extent from 2009 to 2014. The OSCAT extent is compared to SSM/I 0% and 30% mean sea ice extent.

The only Ku-band scatterometer in orbit after the end of the OSCAT mission is operated by the Chinese (the HY2A Scatterometer). Unfortunately, this data is not currently accessible. Further exploration is being done on expanding the data set using C-band scatterometer data.

CHAPTER 4. ASCAT SEA ICE ALGORITHM

4.1 ASCAT Azimuth Modulation

Because of the desire for a continued sea ice extent data set following the end of the OSCAT mission, a new ASCAT sea ice extent algorithm is developed based, in part, on Steven Reeves's work [13]. Operating at C-band, ASCAT σ^0 measurements do not discriminate between sea ice and ocean water as well as Ku-band instruments [9]. Therefore, several sea ice extent algorithms have been developed that combine ASCAT data with passive radiometer data. While combining instruments is effective in discriminating between sea ice and ocean, this method makes it difficult to run a real-time algorithm because it relies on continual operation of all the sensors.

Despite the discrimination challenge of C-band instruments, ASCAT data can stand alone in a sea ice extent algorithm because of the different azimuth angles of its three antennas. A better understanding of the backscatter properties of ocean versus sea ice helps understand the usefulness of comparing the data of the three antennas.

Scatterometers measure the radar backscatter off of wind-formed capillary waves on the ocean surface. The direction of the wind is found by combining the information from antennas fixed at three different azimuth angles. This approach takes advantage of the azimuth modulation of the ocean surface. The antennas receive different levels of backscatter based on their azimuth angle and the angles of the ocean waves.

This is not the case with sea ice. While there are different types and surfaces of sea ice, in general, sea ice has no consistent surface pattern. This results in very little azimuth modulation [25]. By taking the difference between σ^0 backscatter measurements of the different antennas, discrimination between sea ice and ocean becomes more distinguishable.

4.2 Normalized Difference Image

Steven Reeves [13] used the fore and aft antennas to create a normalized difference image from ASCAT data, i.e., for each pixel the ratio

$$d = \frac{\left|\sigma_F^0 - \sigma_A^0\right|}{\left|\sigma_F^0 + \sigma_A^0\right|}, \tag{4.1}$$

is computed where σ_F^0 is the backscatter measurement from the fore antenna and σ_A^0 is the backscatter measurement of the aft antenna. The new approach improves on Reeves's normalized difference by taking advantage of all three antennas. The new normalized difference is:

$$d = \max \frac{\left|\sigma_i^0 - \sigma_j^0\right|}{\left|\sigma_i^0 + \sigma_j^0\right|} \text{ where } i \neq j, \tag{4.2}$$

where σ_i^0 refers to the backscatter measurement of the ith antenna and σ_j^0 is the backscatter measurement of the jth antenna. This enhances Eq. 4.1 because the third antenna maximizes the azimuthal variation seen over the ocean. The third antenna, however, does not affect the difference over sea ice because there is little azimuth modulation in this region.

These two equations are compared to verify the superiority of the three antenna equation. The comparison is done by taking histograms of σ^0 values from four days of Antarctic ASCAT data at different seasonal points of the year. Sea ice masks derived from OSCAT data on the same days are used to flag ASCAT SIR image pixels as either sea ice or ocean. Histograms of water and ice pixel σ^0 values for both the three antenna and the two antenna equations are calculated. Figs. 4.1 and 4.2 show these histogram comparisons. Differences are mainly evident in the water histograms. At certain pixels, the normalized difference can potentially be small with only two antennas despite existing azimuth differences. These azimuth differences are better seen with the three antenna equation. In each figure, the mean of the water histogram is displaced further from the sea ice histogram. This gives a greater discrepancy between water pixels and ice pixels.

Seasonal histograms help display how the histograms change throughout the year. The austral summer is a particularly difficult time period to classify sea ice and ocean pixels because much of the sea ice is melting. This causes similarities between the σ^0 measurements of ocean

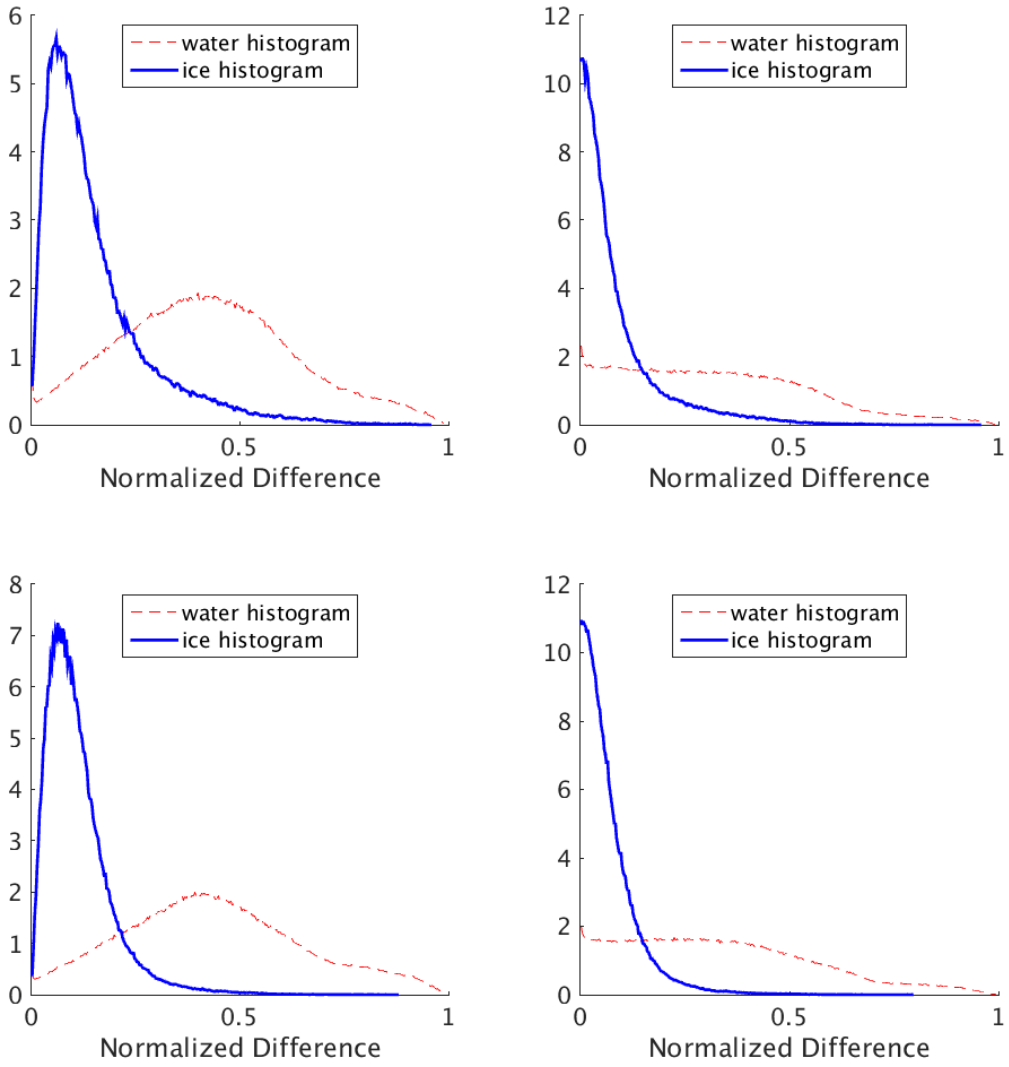

Figure 4.1: ASCAT sea ice and ocean histograms from the three antenna equation (left) and the two antenna equation (right). Data are taken from day 30 (top) and day 120 (bottom) of year 2013.

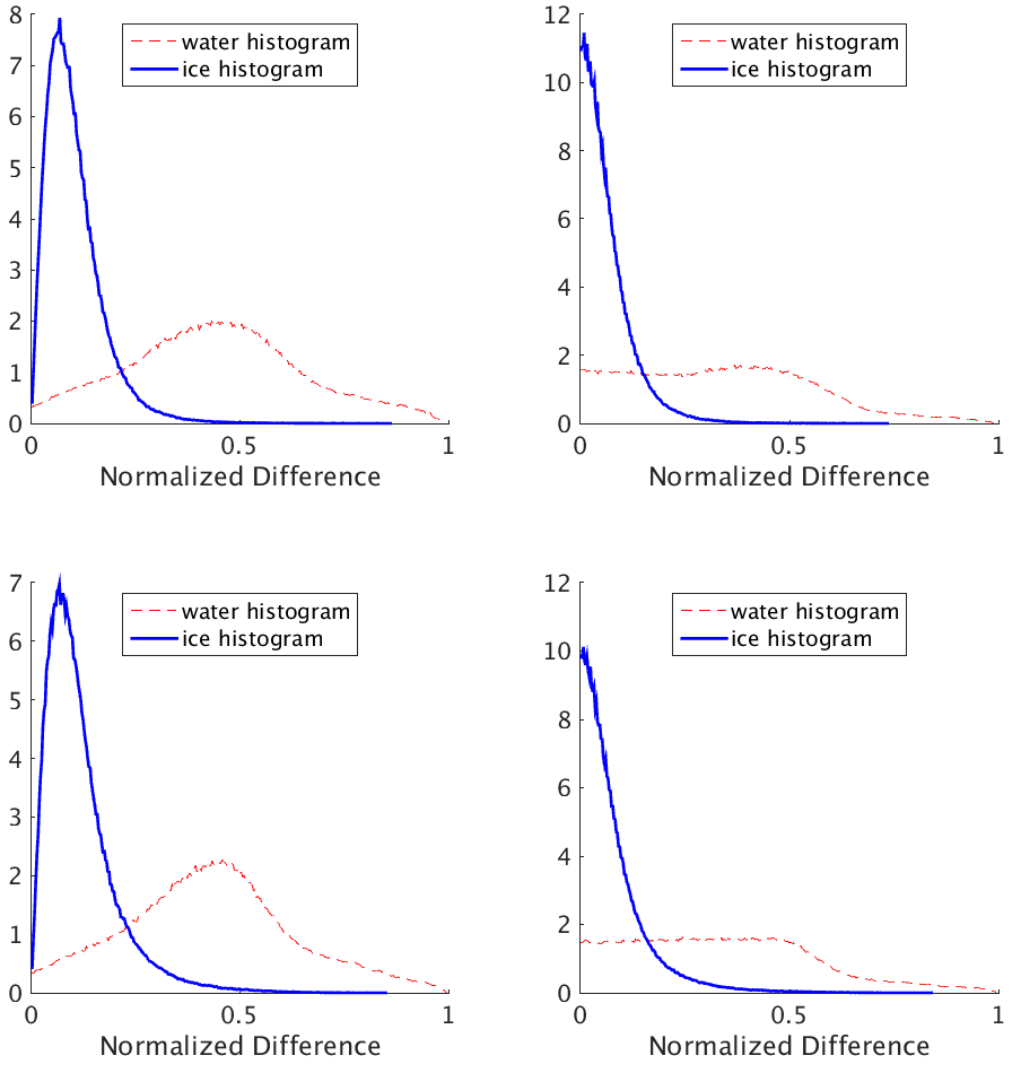

Figure 4.2: ASCAT sea ice and ocean histograms from the three antenna equation (left) and the two antenna equation (right). Data are taken from day 210 (top) and day 300 (bottom) of year 2013.

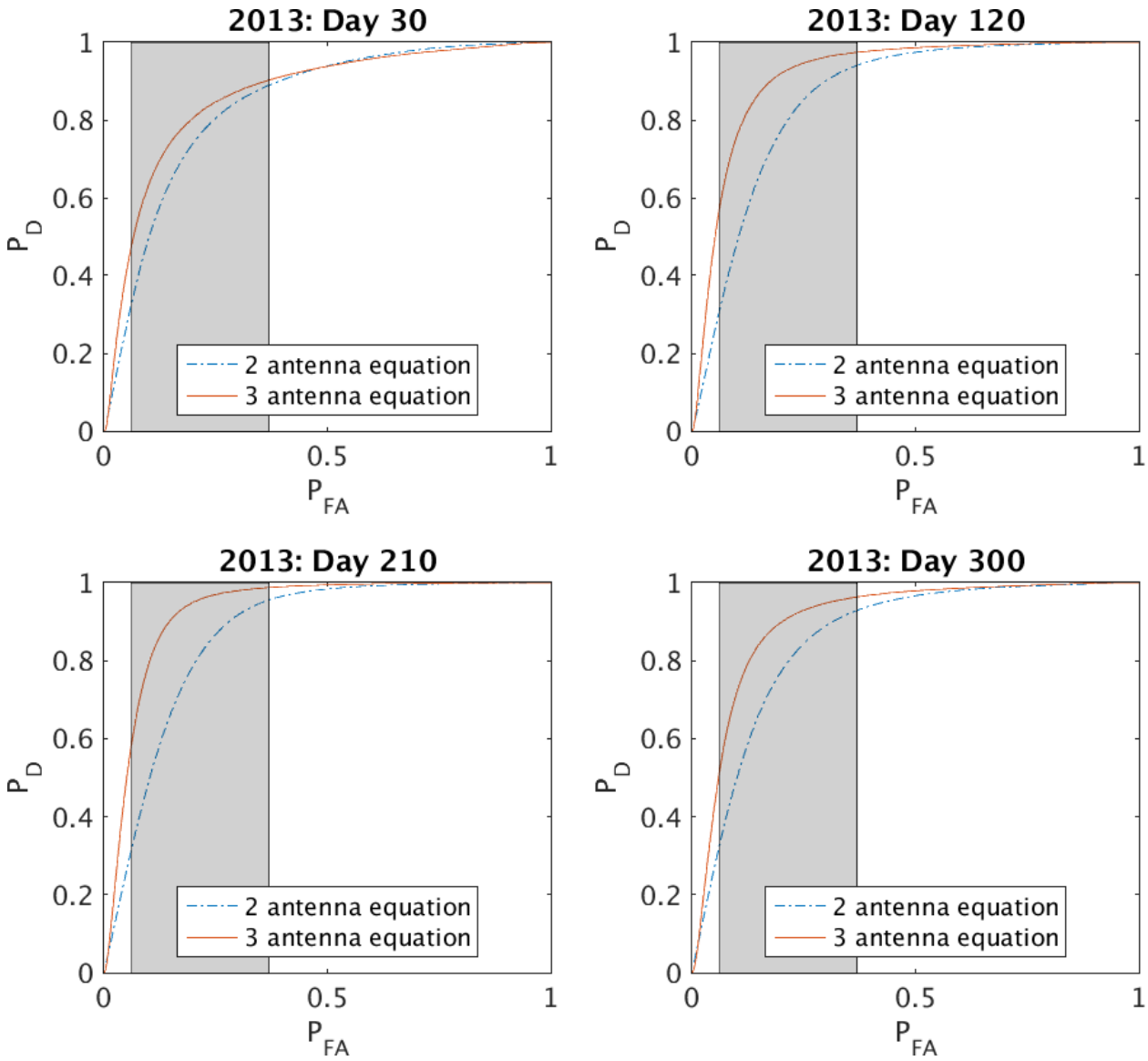

Figure 4.3: Receiver Operating Characteristic (ROC) curves generated from the histograms in Figs. 4.1 and 4.2. Regions of interest are highlighted in gray.

and sea ice at the sea ice edge. Fig. 4.1 shows histograms during this melt season. The two antenna equation histograms shows a heavy overlap between ocean and sea ice. The three antenna equation histograms show improved separation of sea ice and ocean and are therefore better suited for discrimination.

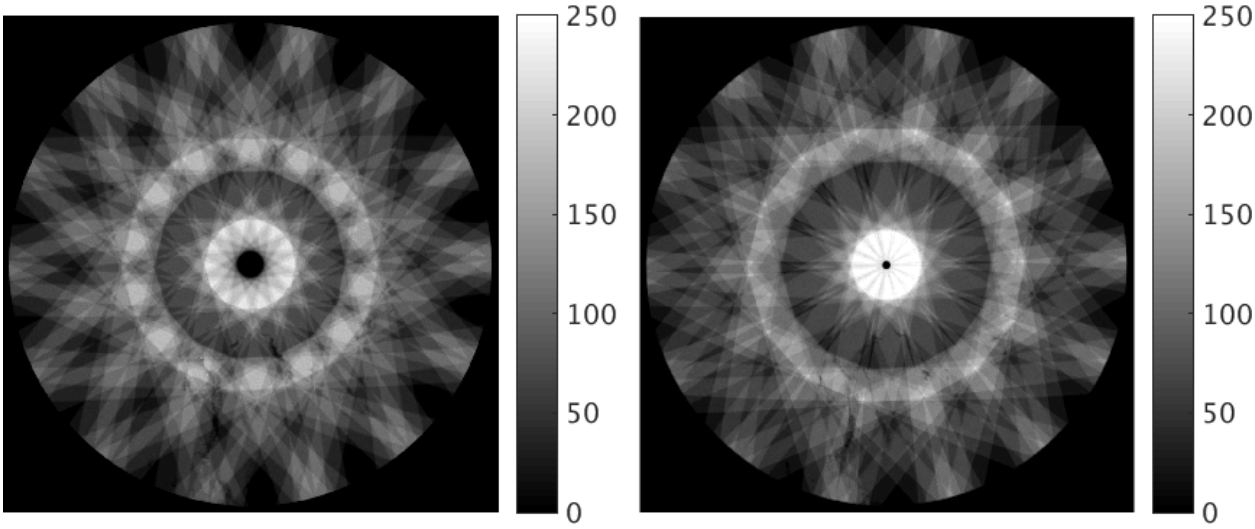

Figure 4.4: ASCAT coverage images for the aft and fore (left) and mid (right) antennas. Pixel values are the number of measurements over the time period of the SIR image. These images are from days 195 and 196 of 2013.

4.2.1 Likelihood Ratio Test

With the histograms modeled as distributions, they are used as inputs to a likelihood ratio test. The ice or water classification is defined by parameter ω where ω_0 is an ocean classification and ω_1 is a sea ice classification. A likelihood ratio test determines the best threshold to use in a simple binary hypothesis test. This hypothesis test determines a binary classification based on the pixel value in relation to the threshold value. The likelihood ratio test is defined as

$$\phi(\mathbf{x}) = \begin{cases} \text{ocean} & l(\mathbf{x}) > k \\ \text{sea ice} & l(\mathbf{x}) < k \end{cases}, \tag{4.3}$$

where $l(\mathbf{x})$ is the likelihood ratio

$$l(\mathbf{x}) = \frac{f_{\omega_1}(\mathbf{x})}{f_{\omega_0}(\mathbf{x})} \tag{4.4}$$

and $f_{\omega_i}(\mathbf{x})$ is the distributions of ocean and sea ice. A false alarm occurs when a pixel is classified as ocean when it should have been classified as sea ice. False alarms are unavoidable in a simple binary hypothesis test when the distributions overlap as they do with the normalized difference equations.

Although a more sophisticated Bayesian approach, described later on, is used to classify sea ice using ASCAT data, the advantage of the three antenna normalized difference equation compared to the two antenna normalized difference equation is shown in their respective Receiver Operating Characteristics (ROC) curves. The ROC curve shows the probability of detection versus the probability of false alarm for every possible threshold k from the maximum likelihood Eq. 4.3. A diagonal line of slope one in a ROC curve would be a chance line meaning the classification of each pixel would be a pure guess. The closer the ROC curve gets to zero probability of false alarm and a unit probability of detection, or in other words the more convex the ROC curve is, the better the parameter is for discrimination. ROC curves for the four days used for histogram comparison are shown in Fig. 4.3. In each figure, the three antenna equation ROC curve is more convex than the two antenna equation ROC curve as desired. The ROC curve from day 30 shows an overlap where the two antenna equation performs better than the three antenna equation. Therefore a threshold chosen in the overlap region would generate better detection statistics from the two antenna equation than the three antenna equation. However, thresholds chosen in this region are not considered because of the high probabilities of false alarm. Areas shaded in gray in Fig. 4.3 are more heavily considered in the comparison between the two equations. In these regions, the three antenna equation outperforms the two antenna equation in detection statistics. This shows the increased discrimination possibilities of the three antenna equation compared to the two antenna equation.

The ROC curve from day 30 shows an overlap where the two antenna equation performs better than the three antenna equation. This shows that a threshold chosen in the overlap region would generate better detection statistics from the two antenna equation than the three antenna equation. However, thresholds chosen in this region are not considered because of the high probability of false alarm. Areas shaded in gray in Fig. 4.3 are more heavily considered in the comparison between the two equations. In these regions, the three antenna equation outperforms the two antenna equation in detection statistics.

4.2.2 ASCAT Coverage Correction

A noticeable disadvantage of the three antenna equation for the normalized difference image is in regards to the instrument coverage of the Earth's surface. The fore and aft antennas cover

more of the polar regions than the mid antenna. In the region of discrepancy where the fore and aft antennas cover but the mid antenna does not, the normalized difference equation with three antennas does not perform as well as areas of full coverage. Therefore the ASCAT coverage (C) image is used to mask out these areas of discrepancy. A threshold is selected for minimum coverage. If a pixel does not meet the coverage threshold then it is not included in the Bayesian classification. Fig. 4.4 shows the coverage of the aft and fore antennas on the left and the coverage of the mid antennas on the right.

4.3 ASCAT Sea Ice Mask Algorithm

The three antenna normalized difference images are included with three other ASCAT images, shown in Fig. 4.5, to drive the ASCAT sea ice extent Bayesian decision algorithm. The decision rule is defined as:

$$\phi(\mathbf{x}) = \begin{cases} \text{sea ice}, & \text{if } p(\mathbf{x}|\omega_1)P(\omega_1) > p(\mathbf{x}|\omega_0)P(\omega_0), \\ \text{ocean}, & \text{otherwise}, \end{cases} \tag{4.5}$$

where $\mathbf{x}$ is the feature vector, ω_0 is ocean classification, ω_1 is sea ice classification, $p(\mathbf{x}|\omega_i)$ is the conditional PDF of $\mathbf{x}$ given the classification, and $P(\omega_i)$ is the prior probability for that classification based on the prior day sea ice mask. The steps of the algorithm for each day are outlined as follows:

1. The four ASCAT parameter images and the previous day ASCAT sea ice mask are collected. If an ASCAT sea ice mask does not exist for the previous day then an OSCAT sea ice mask is used when available. If neither of these are available, a sea ice mask from any sensor on the same Julian day as the previous day of any year is used as the previous day mask.

2. The Prior Probability Map (PPM) is created from the previous day sea ice mask.

3. The data from the four parameter images are normalized to zero mean, unit variance.

4. A conditional multivariate Gaussian PDF is constructed for the four images for both sea ice and water based on the pixel classifications from the previous day sea ice mask.

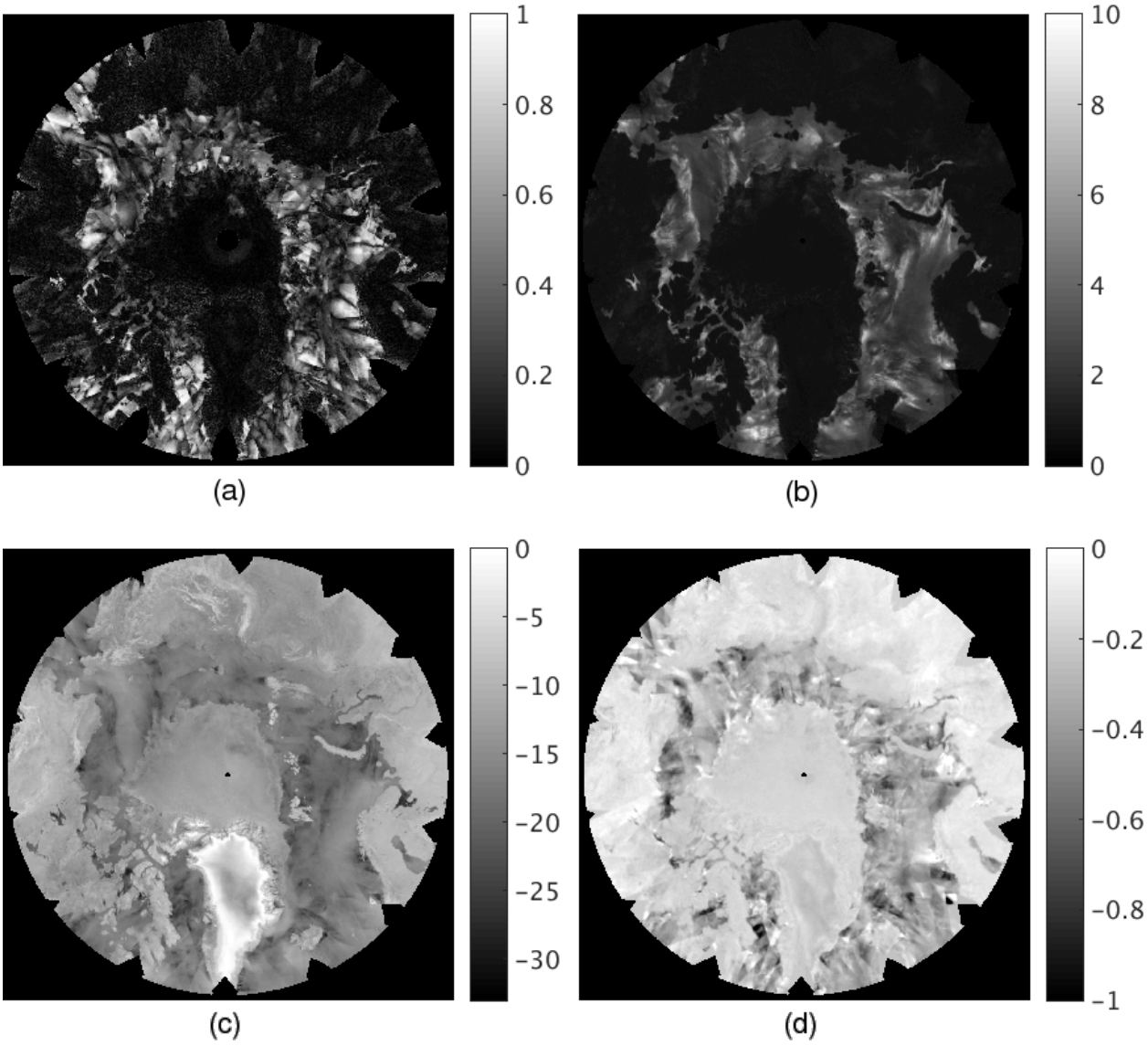

Figure 4.5: The four parameter images included in the ASCAT feature vector. Arctic images are taken from days 280 and 281 in 2012. Images are normalized difference (a), σ^0 standard deviation in dB (b), σ^0 in dB (c), and slope of σ^0 in dB/deg (d).

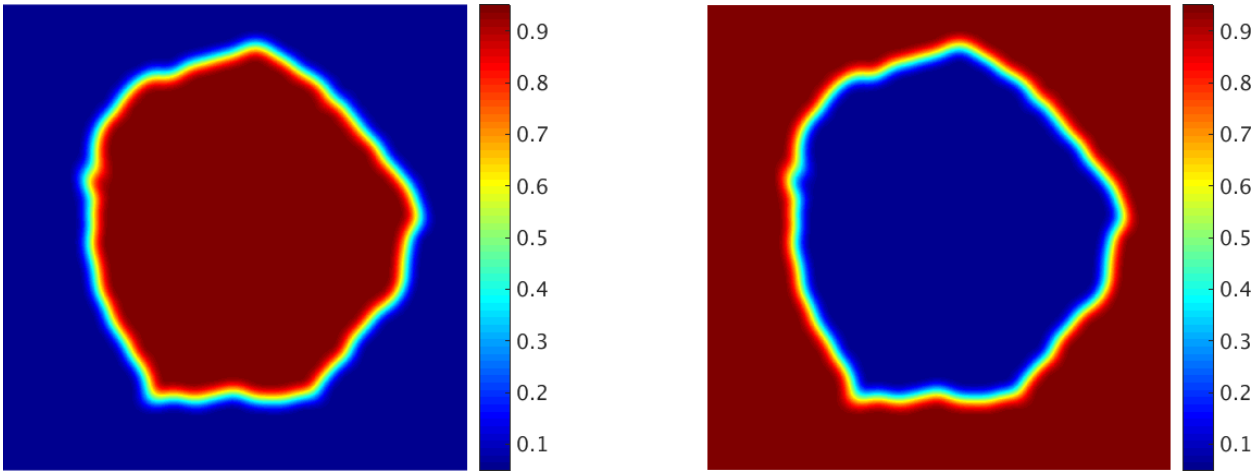

Figure 4.6: PPM for sea ice (left) and ocean (right) on day 195 of 2013.

5. Classify current day pixels as either sea ice or ocean based on the decision rule.

6. Eliminate missed detections and false alarms using image processing techniques.

7. Fill in holes from missing data using previous day sea ice mask.

The four ASCAT parameter images are the A image (σ^0 in dB, typically at 40 degree incidence), the B image (slope of σ^0 in dB/deg), the V image (σ^0 standard deviation image in dB), and the D image (the three antenna normalized difference image discussed previously). The RL algorithm uses the A, B, and V images for QuikSCAT and then later for OSCAT. These three parameters show good discrimination properties for Ku-band instruments. They are less effective for the C-band ASCAT but when combined with the three antenna D image in a multivariate Gaussian model, the discrimination properties are improved.

The previous day sea ice mask is used in two ways. First, it is used to derive the PPM for the current day. The PPM assigns a probability of a certain classification to each pixel. Because the growth and retreat of sea ice in the polar regions is fairly predictable, it is assumed that most pixels classified as ocean in the previous day remain classified as ocean in the current day and most pixels classified as sea ice in the previous day remain classified as sea ice in the current day. Thus, the PPM for sea ice assigns ocean pixels with a value of 0.05 and assigns sea ice pixels with a value of 0.95. The PPM is smoothed by convolving the image with a two dimensional square Gaussian kernel with a standard deviation of fifty pixels to smooth the probabilities around the sea ice edge

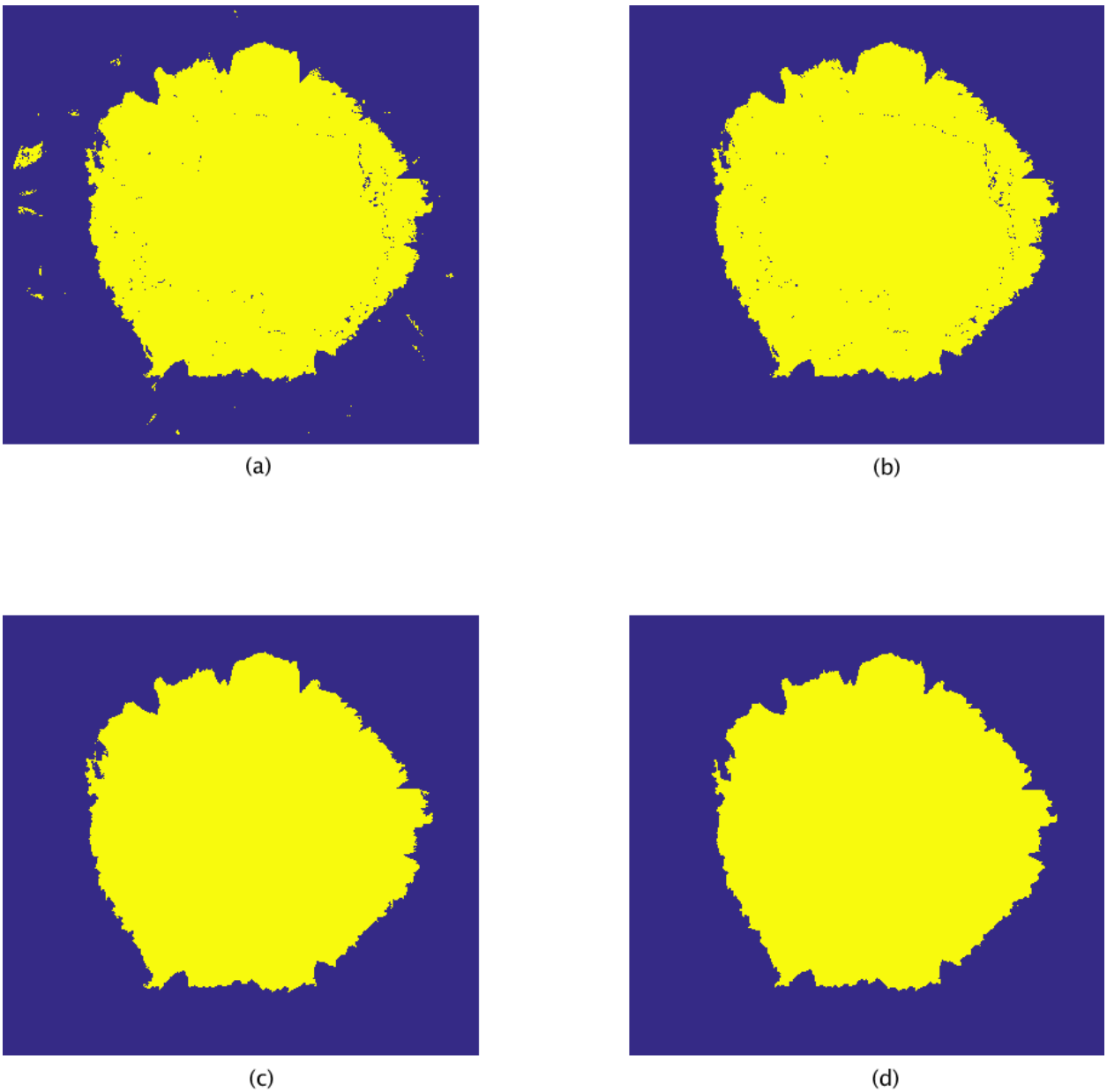

Figure 4.7: ASCAT sea ice masks after initial Bayesian classification processing and various image processing steps. These images comes from ASCAT data from days 195 and 196 of 2013.

where sea ice movement is expected to happen from day to day. Fig. 4.6 shows PPMs from day 195 of 2013 in the Antarctic region for both sea ice and ocean.

The previous day ASCAT sea ice mask is also used for generating the conditional PDFs used in the decision model. The previous day mask has three classifications: water, sea ice, and land. The corresponding pixel locations in the four feature images associated with both the water

and the sea ice classifications from the mask are grouped together. The distributions for both classes are assumed to be Gaussian. The conditional mean and covariance for ocean pixels are calculated. The same is done for sea ice. These are used to form a multivariate Gaussian pdf

$$p(\mathbf{x}|\omega_i) = \frac{1}{(2\pi)^{n/2}|\Sigma_{\omega_i}|^{1/2}}\exp[-\frac{1}{2}(\mathbf{x}-\mu_{\omega_i})^T\Sigma_{\omega_i}^{-1}(\mathbf{x}-\mu_{\omega_i})], \tag{4.6}$$

where μ_{ω_i} is the conditional mean and Σ_{ω_i} is the conditional covariance matrix of $\mathbf{x}|\omega_i$. Each pixel is given a probability of sea ice or ocean based on this conditional pdf. These probabilities are multiplied by the probability associated with its pixel location as defined in the conditional PPMs for that day. These two values are compared as defined in Eq. 4.5 to give the classification for each pixel for the current day.

This initial classification results in a binary image. Because of high winds found at times over the ocean and melt water on the sea ice surface, misclassifications occur from the Bayesian classification process. These misclassifications are corrected using various image processing techniques. The first technique is a region growing method [3]. This eliminates isolated regions of pixels misclassified as ice in the ocean. In both the Arctic and Antarctic, known land pixels are used as a starting point. Neighboring pixels to the land mass classified as ice are added to the region. This process continues until the ice edge is reached. All other pixels outside of this edge are classified as ocean. Stages of this correction technique are shown in Fig. 4.7. Image (a) shows an image of Antarctica following an initial Bayesian classification step. The region growing technique is applied to image (a) to produce image (b).

The next step is a hole filling process that classifies all pixels inside the ice edge as ice. This misclassifies actual holes of water in the ice known as polynyas, but since the goal is to classify the sea ice extent, this misclassification is acceptable. Image (c) of Fig. 4.7 shows the ice extent following the hole filling process.

The resulting masks generally have a high frequency edge which can be smoothed and corrected using a series of erosion and dilation steps [3]. Binary image erosion is an image processing technique that analyzes neighboring pixels and reclassifies the focused pixel based on the neighboring pixels. In this case of erosion, a disk of radius five pixels is used to analyze the neighboring pixels of each pixel in the image. If any of the pixels inside the disk is classified as ocean then the

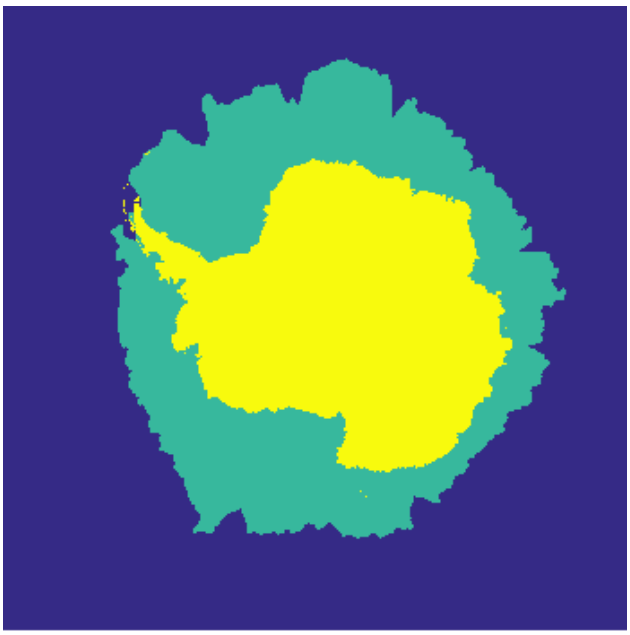

(a)

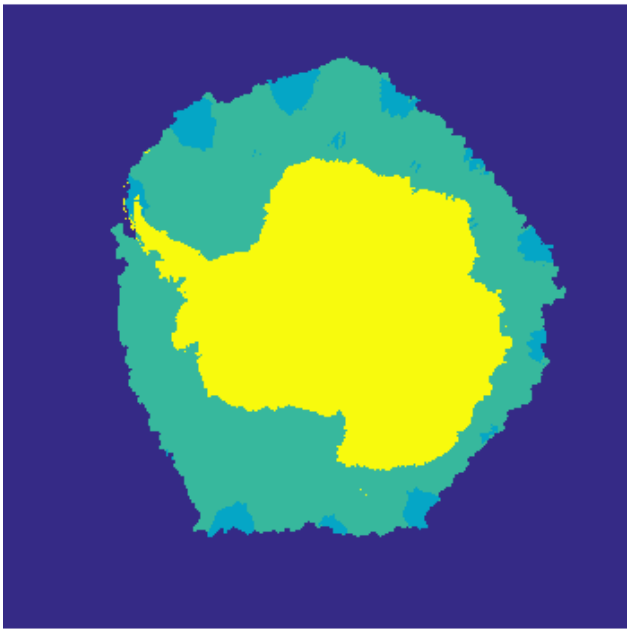

(b)

Figure 4.8: ASCAT sea ice masks before (a) and after (b) filling in empty pixels from lack of swath coverage. These images come from Antarctic ASCAT data from days 195 and 196 of 2013.

pixel of interest is classified as ocean. This process erodes and smooths the sea ice edge. The result of this process is shown in image (d) of Fig. 4.7. This process disconnects many false extrusions from the ice edge.

An additional region growing process is applied to eliminate the new isolated misclassified ice areas in the ocean. A dilation process is then applied to the image. This process is the opposite of the erosion technique. A disk of radius five pixels is used to analyze neighboring pixels of the pixel of interest. If any pixel in the disk is classified as ice then the pixel of interest is reclassified as ice.

Following the image processing techniques, the land mask is used to outline the land in the ice mask. This creates the trinary mask consisting of ocean, sea ice, and land. The final step is to fill in the holes that result from lack of ASCAT swath coverage in the polar regions. It is assumed that sea ice growth and retreat day to day is relatively small compared to the total extent. Therefore, the previous day mask is used to fill in the missing data. If pixels in the current day hole are classified as ice in the previous day mask then they are also classified as ice in the current day mask. An example of this process is shown in Fig. 4.8. Image (a) is shown with the holes present. Image (b) shows the holes filled and these pixels highlighted in a different color.

4.4 Results

ASCAT data from both polar regions from 2010 to 2013 are processed using the ASCAT Bayesian classification algorithm. Representative sea ice extent masks are shown in Figs. 4.9 and 4.10. These masks are shown in comparison to a parameter image used in processing. Visually, the sea ice extent in the mask matches the extent in the parameter image. Further validation with other instruments and algorithms is required, however, to prove the Bayesian classification algorithm.

The ASCAT sea ice extent data set overlaps with the OSCAT sea ice extent data set. ASCAT sea ice extent data is validated with the OSCAT sea ice extent data. This is done by tracking daily total sea ice extent for both data sets. Pixels flagged as sea ice are multiplied by the 4.5-km pixel size of the polar stereographic projection to compute the total sea ice extent area. The ASCAT and OSCAT areas are compared for the same days in Figs. 4.11 and 4.12.

This data also overlaps with SSM/I data. The NASA Team algorithm, discussed previously, is used to generate daily sea ice masks of the polar regions. This data is also used to validate

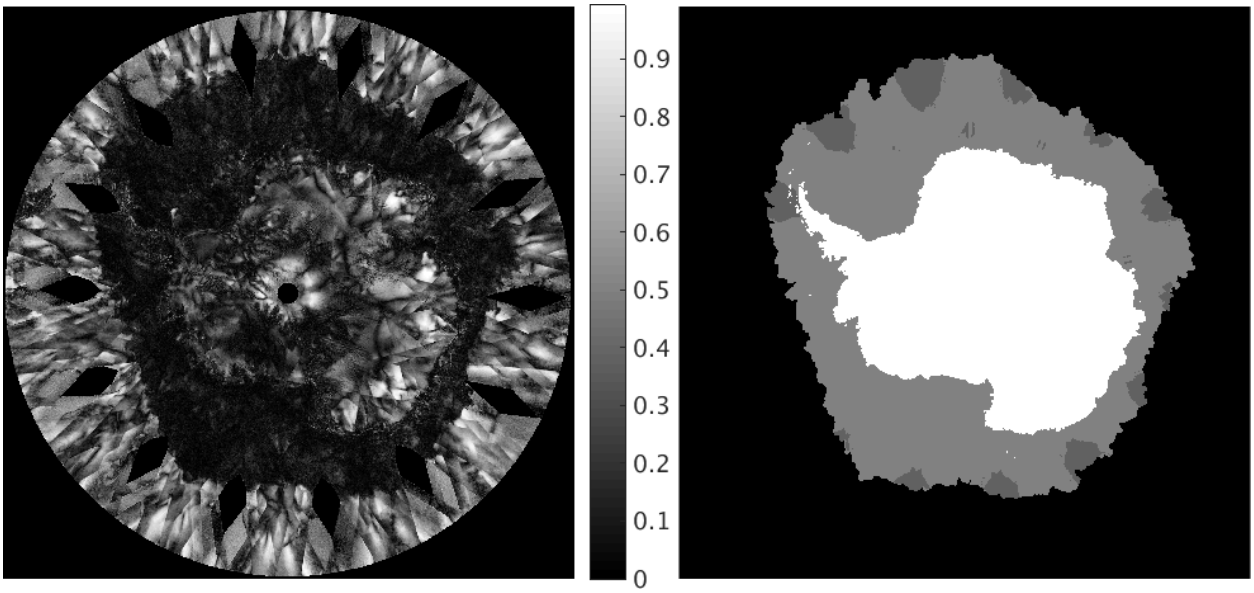

Figure 4.9: ASCAT Antarctic ice mask from day 224 of 2011 (right). The three antenna normalized difference image for that day is shown for comparison (left).

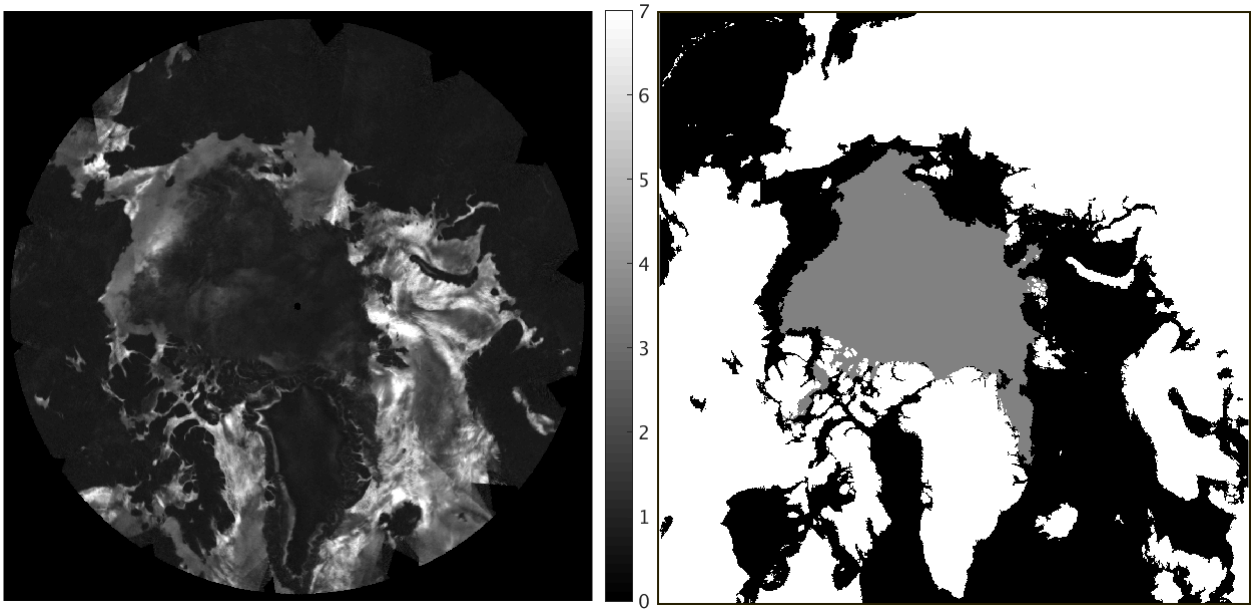

Figure 4.10: ASCAT Arctic ice mask from day 224 of 2011 (right). ASCAT V image (σ^0 standard deviation in dB) for that day is shown for comparison (left).

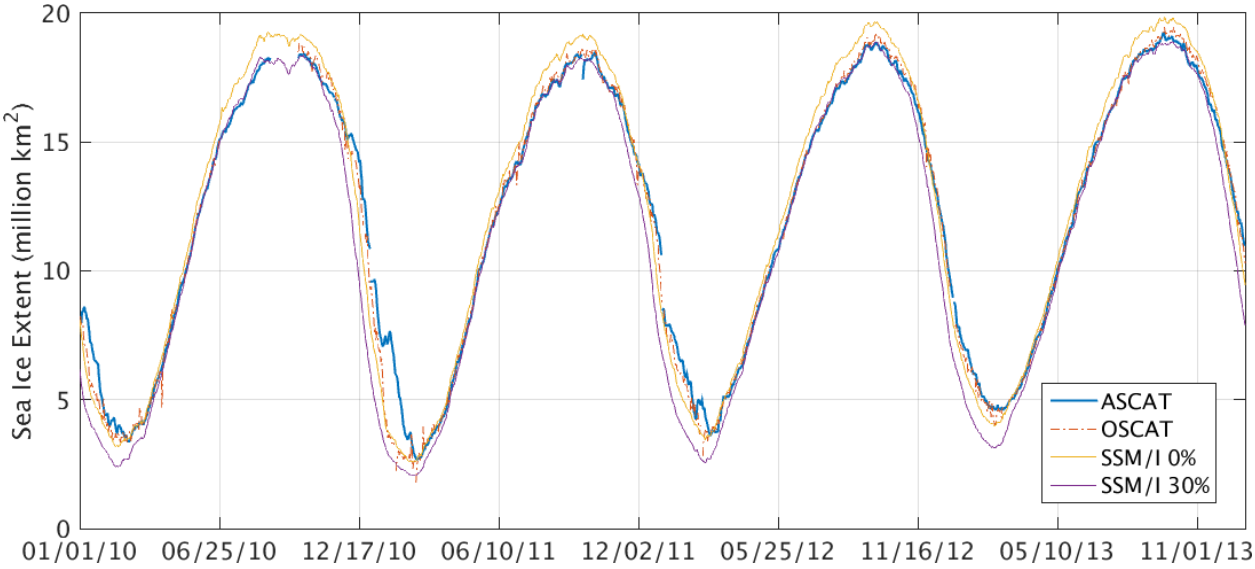

Figure 4.11: Sea ice extent comparison between ASCAT, OSCAT, and SSM/I data sets from 2010 to 2013 in the Antarctic.

ASCAT sea ice extent data. Scatterometer sea ice extent data is only measured north of 60° N latitude. SSM/I data used in the comparison is reduced to the same spatial area. The NASA Team algorithm reports a percent concentration of ice for each pixel. ASCAT data is compared to the 0% and the 30% sea ice concentration masks. All pixels with sea ice percent concentrations above the sea ice concentration threshold are included in the sea ice extent. The total extent of sea ice, measured in square kilometers, in both polar regions are tracked from 2010 through 2013 and plotted in Figs. 4.11 and 4.12.

The results of this comparison are similar to previous comparisons for OSCAT and QuikSCAT [3,34]. Arctic sea ice extents measured with scatterometer data tend to be smaller in the winter and larger in the summer than radiometer sea ice extent data. This behavior is displayed in ASCAT sea ice extent data as well. This is likely the result of differing properties measured by scatterometers and radiometers. Emissivity and backscatter differ during sea ice melt and freeze periods causing differences in sea ice measurements during these times between scatterometer and radiometer data [34]. Apart from slight biases during melt periods, the ASCAT sea ice extent data set is comparable with OSCAT and NASA Team sea ice extent data.

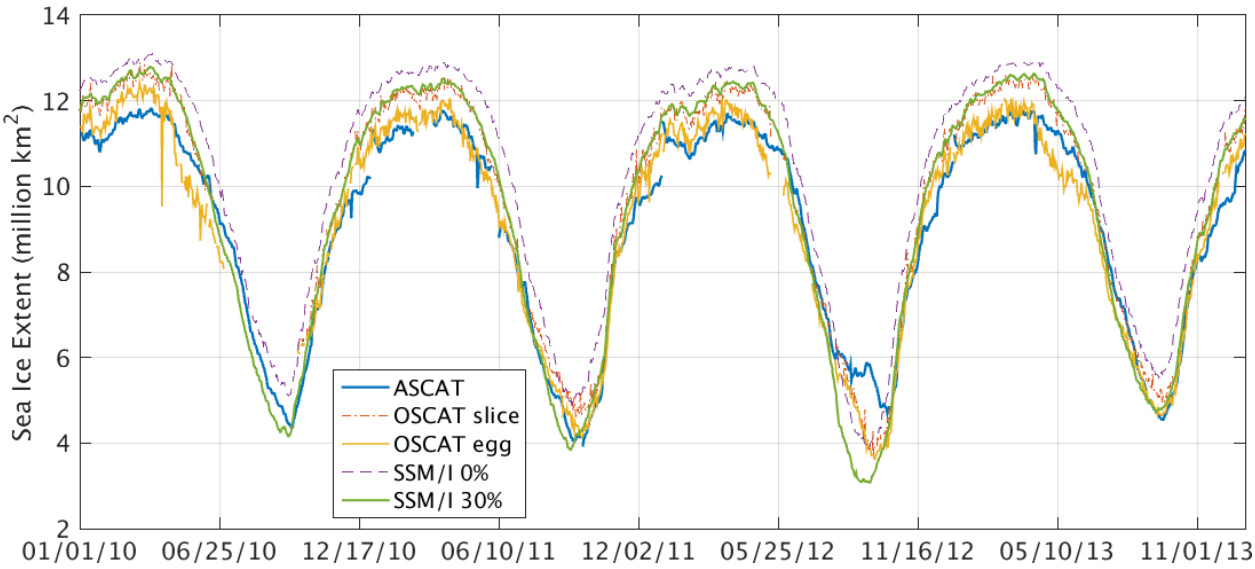

Figure 4.12: Sea ice extent comparison between ASCAT, OSCAT, and SSM/I data sets from 2010 to 2013 in the Arctic.

4.5 Conclusion

The Bayesian classification sea ice extent algorithm for ASCAT is developed to continue the scatterometer sea ice extent data set. Normalized difference images are developed using azimuthal difference between different antenna measurements. The normalized difference images using three antennas are shown to be more useful in discriminating between sea ice and ocean than the normalized difference images that use only data from the fore and aft antennas. Post processing techniques are employed to smooth the ice edge.

The ASCAT sea ice extent data set is validated to overlapping OSCAT and SSM/I sea ice extent data. Yearly trends between the data sets show that the ASCAT sea ice extent data set contributes to the independent scatterometer sea ice extent data set.

CHAPTER 5. CONCLUSION

5.1 Contributions

This thesis builds upon the previous work done in sea ice extent mapping using scatterometers. In order to continue the scatterometer sea ice extent data set, the QuikSCAT sea ice extent algorithm is adjusted for OSCAT and an algorithm is enhanced for ASCAT sea ice extent measurements. Both data sets from the two instruments are validated to previous scatterometer and radiometer data sets. Research contributions described in this thesis are summarized in the following section.

5.1.1 OSCAT Algorithm Reverse Processing

OSCAT has several gaps in its σ^0 data set. Some gaps are hours long, some days long, and one gap lasts several weeks. Because the QuikSCAT sea ice extent algorithm uses the previous day's sea ice mask to constrain sea ice growth and retreat for the current day, it is necessary to adjust the OSCAT algorithm to account for the data gaps in OSCAT data. A reverse processing approach, which uses the following day's mask as the constraint, is implemented following the forward processing approach on data that comes after three days or more of OSCAT data gaps. This properly constrains the growth and retreat during these days.

5.1.2 OSCAT Sea Ice Extent Validation

The OSCAT sea ice extent data set continued the scatterometer sea ice extent data set. It overlaps with the QuikSCAT sea ice extent data set for eighteen days. These days are used to verify the algorithm's capability on OSCAT data. The remaining OSCAT data set is validated with SSM/I 0% and 30% sea ice extent data sets.

5.1.3 ASCAT Normalized Difference Images

As a C-band instrument, ASCAT σ^0 measurements of sea ice are not as distinguishable from ocean measurements as Ku-band scatterometer σ^0 data are. The A, B, and V ASCAT images do not yield very much information to build a sea ice extent algorithm around. A normalized difference image uses the azimuthal differences between the fore, aft, and mid antennas. The normalized difference images are used as another data vector in the input to the Bayesian sea ice classification algorithm.

5.1.4 ASCAT Coverage Images

The fore, aft, and mid antennas have different Earth coverage patterns. The normalized difference measurements are not as accurate over areas of less swath coverage. Areas with no ASCAT coverage are already eliminated from SIR images. However, in order to improve the usability of the normalized difference images, it is beneficial to remove areas that have only minimal swath coverage as well. These areas are determined by ASCAT coverage images from the fore, mid, and aft antennas of the current day being processed. If a pixel does not have sufficient coverage its data is removed from processing. These areas are later filled in using previous day masks.

5.1.5 ASCAT Sea Ice Extent Validation

The ASCAT sea ice extent data set also continues the scatterometer data set. It overlaps with QuikSCAT and OSCAT allowing for validation with both instruments. It is also compared to SSM/I sea ice extent data sets.

5.2 Future Work

While much progress has been made, there is room for additional work. The possible research expansion beyond this thesis is discussed in the following subsections.

5.2.1 Unified Scatterometer Sea Ice Extent Algorithm

Several sea ice extent algorithms have been developed for each scatterometer. Few of these have been applied to different scatterometer data than the one intended for the algorithm. A valuable study would be to use one sea ice extent algorithm for all scatterometer data previously available until the present. The only adjustments between scatterometers would be the input feature images.

5.2.2 OSCAT Sea Ice Extent Algorithm for OSCAT-2

ISRO recently launched the OSCAT-2 mission to continue OSCAT data following the end of the original OSCAT mission. The OSCAT sea ice extent algorithm could be applied to data from this new sensor. It may not need the reverse processing approach if the sensor data is more reliable than before.

5.2.3 Digital Image Processing Verification

Several scatterometer sea ice extent algorithms use digital image processing techniques to correct misclassifications and smooth the sea ice extent edge. The results of these processing steps are difficult to verify. High resolution SAR images of the ice edge surface are needed to validate the sea ice edge after image processing techniques are applied. A thorough study of SAR images compared to scatterometer sea ice extent data would help validate the edge results.

REFERENCES

[1] Bradley, J. P., and Long, D. G., 2014. "Estimation of the OSCAT spatial response function using island targets." *Geoscience and Remote Sensing, IEEE Transactions on,* **52**(4), pp. 1924–1934.

[2] Lindsley, R. D., Anderson, C., Figa-Saldaña, J., and Long, D. G., 2016. "A parameterized ascat measurement spatial response function." *IEEE Transactions on Geoscience and Remote Sensing,* **54**(8), pp. 4570–4579.

[3] Remund, Q. P., and Long, D. G., 1999. "Sea ice extent mapping using Ku band scatterometer data." *Journal of Geophysical Research: Oceans,* **104**(C5), pp. 11515–11527.

[4] Naderi, F. M., Freilich, M. H., and Long, D., 1991. "Spaceborne radar measurement of wind velocity over the ocean-an overview of the NSCAT scatterometer system." *Proceedings of the IEEE,* **79**(6), pp. 850–866.

[5] Long, D. G., Drinkwater, M. R., Holt, B., Saatchi, S., and Bertoia, C., 2001. "Global ice and land climate studies using scatterometer image data." *Eos, Transactions American Geophysical Union,* **82**(43), pp. 503–503.

[6] Long, D. G., and Drinkwater, M. R., 1999. "Cryosphere applications of NSCAT data." *Geoscience and Remote Sensing, IEEE Transactions on,* **37**(3), pp. 1671–1684.

[7] Parkinson, C. L., Comiso, J. C., Zwally, H. J., Cavalieri, D. J., Gloersen, P., and Campbell, W. J., 1987. "Arctic sea ice, 1973-1976: Satellite passive-microwave observations.".

[8] Comiso, J. C., Cavalieri, D. J., Parkinson, C. L., and Gloersen, P., 1997. "Passive microwave algorithms for sea ice concentration: A comparison of two techniques." *Remote sensing of Environment,* **60**(3), pp. 357–384.

[9] Ulaby, F. T., Long, D. G., Blackwell, W. J., Elachi, C., Fung, A. K., Ruf, C., Sarabandi, K., Zebker, H. A., and Van Zyl, J., 2014. *Microwave radar and radiometric remote sensing*., Vol. 4 University of Michigan Press Ann Arbor.

[10] Lindell, D., and Long, D. G., 2015. "Multiyear Arctic sea ice classification using OSCAT." *Geoscience and Remote Sensing, IEEE Transactions on*.

[11] Anderson, H. S., and Long, D. G., 2005. "Sea ice mapping method for SeaWinds." *IEEE Transactions on Geoscience and Remote Sensing,* **43**(3), pp. 647–657.

[12] Remund, Q. P., Long, D. G., and Drinkwater, M. R., 2000. "An iterative approach to multisensor sea ice classification." *Geoscience and Remote Sensing, IEEE Transactions on,* **38**(4), pp. 1843–1856.

[13] Reeves, S. J., 2012. "Sea ice mapping using enhanced resolution advanced scatterometer images." Thesis, Brigham Young University-Provo.

[14] Tsai, W., Spencer, M., Wu, C., Winn, C., and Kellogg, K., 2000. "SeaWinds on QuikSCAT: sensor description and mission overview." In *Geoscience and Remote Sensing Symposium, 2000. Proceedings. IGARSS 2000. IEEE 2000 International*, Vol. 3, IEEE, pp. 1021–1023.

[15] Spencer, M. W., Wu, C., and Long, D. G., 2000. "Improved resolution backscatter measurements with the SeaWinds pencil-beam scatterometer." *Geoscience and Remote Sensing, IEEE Transactions on,* **38**(1), pp. 89–104.

[16] SAF, O., 2013. Oceansat-2 wind product user manual Tech. rep., SAF/OSI/CDOP2/KNMI/TEC/MA/140, available on http://www.knmi.nl/scatterometer/osisaf/ accessed on 07 October.

[17] SAF, O., 2013. ASCAT wind product user manual Tech. rep., SAF/OSI/CDOP2/KNMI/TEC/MA/140, available on http://www.osi-saf.org/biblio/docs/ accessed on 06 February.

[18] Gesell, G., 1989. "An algorithm for snow and ice detection using avhrr data an extension to the APOLLO software package." *International Journal of Remote Sensing,* **10**(4-5), pp. 897–905.

[19] Svendsen, E., Kloster, K., Farrelly, B., Johannessen, O., Johannessen, J., Campbell, W., Gloersen, P., Cavalieri, D., and Mätzler, C., 1983. "Norwegian remote sensing experiment: Evaluation of the Nimbus 7 scanning multichannel microwave radiometer for sea ice research." *Journal of Geophysical Research: Oceans,* **88**(C5), pp. 2781–2791.

[20] Emery, W., Fowler, C., and Maslanik, J., 1994. "Arctic sea ice concentrations from special sensor microwave imager and advanced very high resolution radiometer satellite data." *Journal of Geophysical Research: Oceans,* **99**(C9), pp. 18329–18342.

[21] Hollinger, J., Lo, R., Poe, G., Savage, R., and Pierce, J., 1987. "Special sensor microwave/imager users guide." *NRL Tech. Rpt*.

[22] Cavalieri, D., Gloersen, P., and Campbell, W., 1984. "Determination of sea ice parameters with the Nimbus 7 SMMR." *Journal of Geophysical Research: Atmospheres,* **89**, pp. 5355–5369.

[23] Comiso, J. C., 1995. *SSM/I sea ice concentrations using the bootstrap algorithm.*, Vol. 1380 National Aeronautics and Space Administration, Goddard Space Flight Center.

[24] Long, D. G., Hardin, P. J., and Whiting, P. T., 1993. "Resolution enhancement of spaceborne scatterometer data." *IEEE Transactions on Geoscience and Remote Sensing,* **31**(3), pp. 700–715.

[25] Early, D. S., and Long, D. G., 2001. "Image reconstruction and enhanced resolution imaging from irregular samples." *Geoscience and Remote Sensing, IEEE Transactions on,* **39**(2), pp. 291–302.

[26] Remund, Q., and Long, D. G., 2014. "A decade of QuikSCAT scatterometer sea ice extent data." *IEEE Trans. Geosci. Remote Sens.,* **52**(7), pp. 4281–4290.

[27] Russ, J. C., 2011. *The Image Processing Handbook*. CRC press, Boca Raton, FL, USA.

[28] Pratt, W., 1991. *Digital Image Processing*. John Wiley & Sons, New York, NY, USA.

[29] Markus, T., and Cavalieri, D. J., 2000. "An enhancement of the NASA Team sea ice algorithm." *IEEE Transactions on Geoscience and Remote Sensing,* **38**(3), pp. 1387–1398.

[30] Hill, J. C., and Long, D. G., 2017. "Extension of the QuikSCAT sea ice extent data set with OSCAT data." *IEEE Geoscience and Remote Sensing Letters,* **14**(1), pp. 92–96.

[31] Bhowmick, S. A., Kumar, R., and Kumar, A. S. K., 2014. "Cross calibration of the OceanSAT-2 scatterometer with QuikSCAT scatterometer using natural terrestrial targets." *Geoscience and Remote Sensing, IEEE Transactions on,* **52**(6), pp. 3393–3398.

[32] Cavalieri, D., Parkinson, C., Gloersen, P., and Zwally, H., 1997. "Arctic and Antarctic sea ice concentrations from multichannel passive-microwave satellite data sets: October 1978–September 1995: User's guide." *NASA Technical Memorandum 104647*.

[33] Cavalieri, D., Parkinson, C., Gloersen, P., and Zwally, H., 1996, updated yearly. Sea ice concentrations from Nimbus-7 SMMR and DMSP SSM/I-SSMIS passive microwave data. [subset 2009-2014]. Boulder, Colorado USA: NASA National Snow and Ice Center Distributed Active Archive Center.

[34] Meier, W. N., and Stroeve, J., 2008. "Comparison of sea-ice extent and ice-edge location estimates from passive microwave and enhanced-resolution scatterometer data." *Annals of Glaciology,* **48**(1), pp. 65–70.

APPENDIX A. QUIKSCAT POST WIND MISSION SEA ICE DETECTION

A.1 Introduction

Wind scatterometers are used primarily to measure wind speeds over the ocean. Cryosphere applications have been explored as well using the normalized radar cross section (σ^0) of the surface. The Quick Scatterometer (QuikSCAT) was launched by NASA in June 1999. Several studies show the usefulness of QuikSCAT data in sea ice detection and classification.

QuikSCAT is a 13.4 GHz (Ku-band) pencil-beam scatterometer with two beams that rotate measuring h-pol and v-pol. It rotates the Earth in a sun-synchronous orbit. Scatterometers are impervious to cloud cover or lack of sunlight making them especially useful in polar regions where it is often overcast and dark through much of the polar winters. QuikSCAT is designed to measure 90% of the Earth's surface in a single day.

QuikSCAT operated properly through 2009. During this time, several algorithms were applied to QuikSCAT data to measure the sea ice edge and the sea ice age in the Arctic and Antarctic regions. The rotating dish antenna of QuikSCAT stopped spinning on November 23, 2009 due to a bearing failure on the antenna motor. The instrument continues to transmit data, but the coverage of the fixed instrument is not sufficient to measure surface wind vectors. The wind mission of QuikSCAT therefore runs through November 21, 2009. However, NASA did not immediately terminate data transmission following this date. The purpose of this paper is to discuss the possibility of Cryosphere applications using QuikSCAT data collected after November 21, 2009.

A.2 Post Wind Mission

The collection of QuikSCAT data following this date is referred to as QuikSCAT post wind mission (PWM). NASA proposed to continue the collection of data to aid in cross-calibration of other scatterometers. This is possible despite the fixed azimuth angle of the instrument.

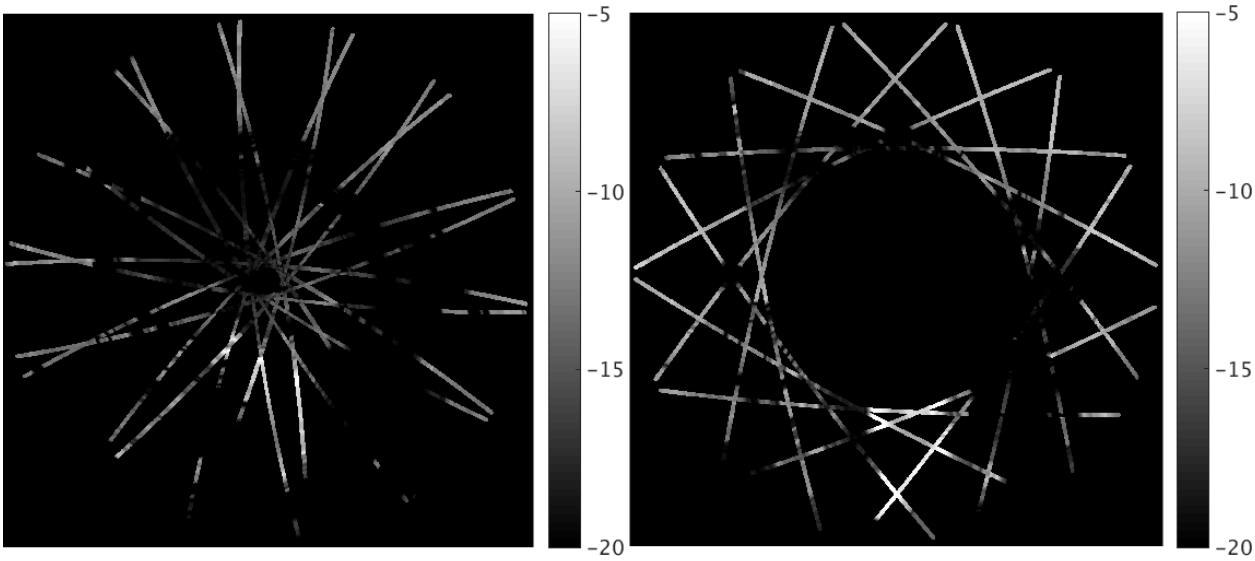

Figure A.1: QuikSCAT PWM SIR images of the Arctic from day 201 of 2010 (left) and day 51 of 2014 (right). The color scale is σ^0 in dB. The temporal difference shows the change in antenna position that happened in between these two dates.

During the PWM data collection, QuikSCAT provides the best spatial coverage over the polar regions. The amount of coverage is still insufficient for wind vector processing, but sea ice applications using PWM data is explorable. One-day QuikSCAT PWM SIR images of the polar regions from 2010 and 2014 are displayed in Figs. A.1 and A.2. Individual passes are easily identifiable in each figure and it is noted that several passes are made each day over each pole. Another important observation is the proximity of each pass to the actual pole. Because of the fixed azimuth angle, closer coverage to the pole is accomplished in one pole more than the other. This is shown in Fig. A.1 where the Arctic region has better coverage closer to the pole in 2010 as compared to 2014 when the azimuth angle had changed after the antenna motor started again and then later stopped permanently. Fig. A.2 shows the difference in polar coverage from earlier after the azimuth angle change.

A.3 Data Averaging

A single day of polar QuikSCAT PWM data is not a sufficient amount of information to determine sea ice age or any other sea ice application. However, QuikSCAT has a four-day repeat orbit with each new repeat cycle starting slightly off of the original position. This enables averaging

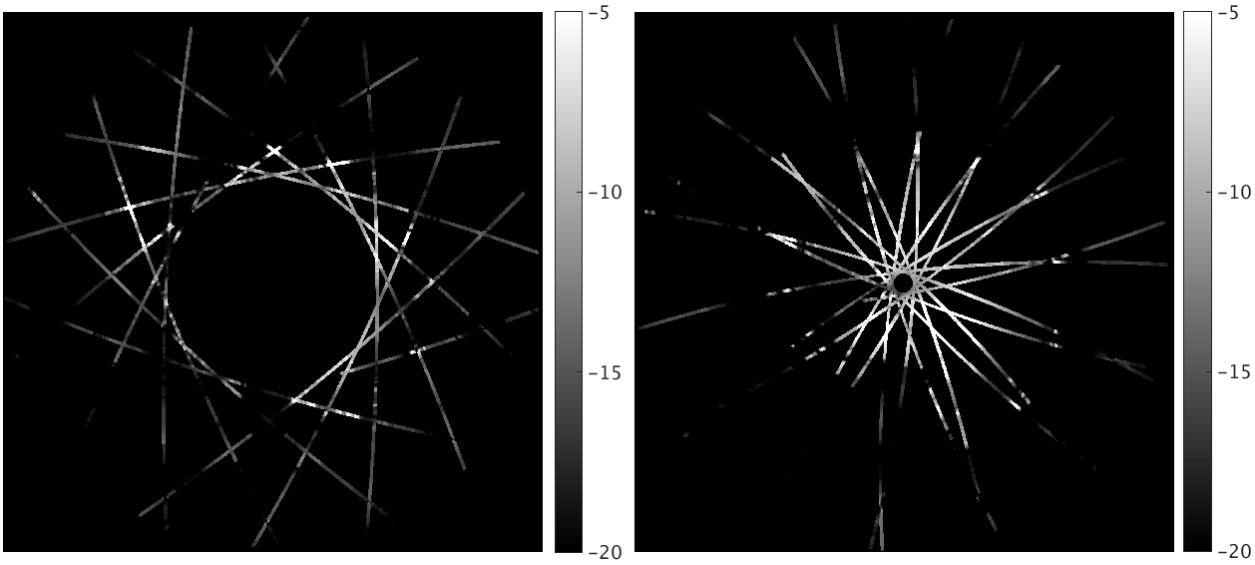

Figure A.2: QuikSCAT PWM SIR images of the Antarctic from day 201 of 2010 (left) and day 51 of 2014 (right). The color scale is σ^0 in dB.

of multiple days of PWM data for greater spatial coverage. The improved spatial resolution comes at the cost of reduced temporal resolution.

This trade-off is displayed in Figs. A.3 and A.4. These images are created by averaging ten one-day σ^0 QuikSCAT PWM images together. Only pixels with data are averaged together. Pixels marked as no data for all ten images are marked as no data for the ten day averaged images. Despite the incomplete data over ten days, the averaged images provide more coverage over the polar regions than one-day or two-day images.

The challenge with the averaged images is the fixed incidence angle. During QuikSCAT's wind mission, all azimuth angles are covered because the instrument rotates conically through all azimuth angles. With the mechanical failure that stopped the rotation of the instrument, QuikSCAT is fixed at one azimuth angle during the post wind mission. However, due to sporadic restarting of the antenna rotation, the azimuth angle changes throughout the post wind mission. This has a significant effect on the polar region coverage of QuikSCAT PWM.

This change in coverage is displayed in Figs. A.3 and A.4. In 2010 the azimuth angle of QuikSCAT causes a large area of missing data at the southern pole. The northern pole in 2010 is mostly covered with only a small area of missing data right at the pole. In 2014 the azimuth angle is changed causing an opposite effect. A large area of missing data is prevalent in the northern

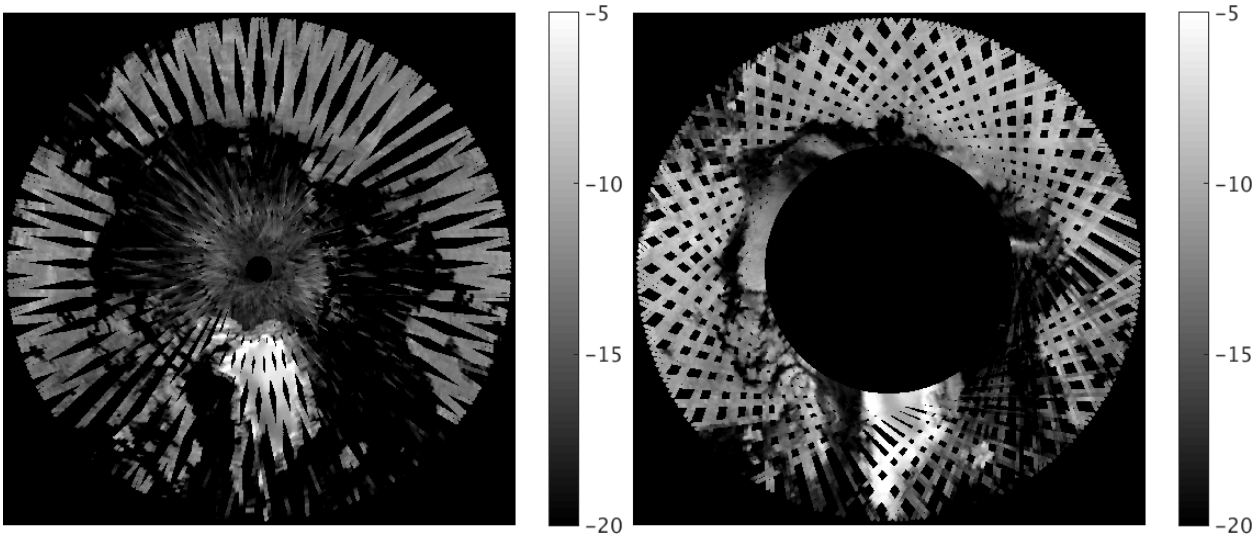

Figure A.3: QuikSCAT PWM SIR images of the Arctic averaged together from day 201 through day 210 of 2010 (left) and from day 50 through day 59 of 2014 (right). The color scale is σ^0 in dB.

pole and only a small area of missing data exists in the southern pole. The ideal scenario for sea ice edge classification is to have the large area of missing data in the southern pole where most of the missing data is known to be land. This allows for minimal loss of sea ice data in the Antarctic region and good coverage of sea ice data in the Arctic region. This ideal situation exists in 2010.

A.4 Sea Ice Edge Classification Using QuikSCAT PWM Data

It is hypothesized that despite the lack of coverage of QuikSCAT PWM data, the RL-N sea ice edge detection algorithm adapted for QuikSCAT, discussed previously, could be applied to PWM data and produce satisfactory results for comparison with other scatterometer sea ice edge data sets. The use of PWM data requires finding the right balance between available data and ice edge movement. More days of data can be averaged together to improve coverage; however, sea ice extent grows or retreats further over more days making it more difficult to distinguish the ice edge.

In testing different day ranges of data, it is found that ten days of data produces a plausible amount of coverage to justify running a sea ice extent algorithm on this amount of data. Ranges longer than this smear the ice edge too much and ranges shorter do not give enough coverage. Data

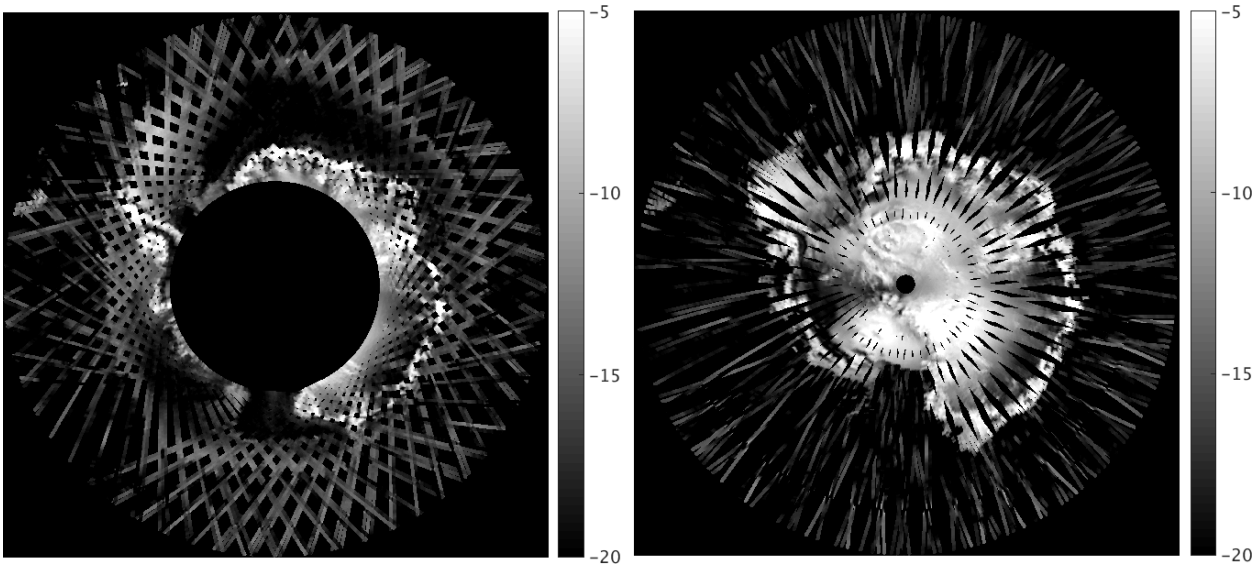

Figure A.4: QuikSCAT PWM SIR images of the Antarctic averaged together from day 201 through day 210 of 2010 (left) and from day 50 through day 59 of 2014 (right). The color scale is σ^0 in dB.

from the Arctic, when the antenna points away from the north pole, are discarded due to the large coverage gap over the pole during these days.

Available data from 2010 and 2014 are run through the RL-N algorithm applied to QuikSCAT. Coverage gaps inside the extent are filled in, but gaps on the sea ice edge are unaccounted for. Fig. A.5 shows the sea ice mask generated from data from days 201 to 210 in 2010. It is compared side by side with an ice mask from operating QuikSCAT data from day 201 in 2009. The protrusions on the sea ice edge of the PWM data represent just one of the challenges with lack of data and coverage in classifying sea ice extent with PWM data.

A.5 Conclusion

It is found that despite the larger coverage with a ten day range of data, there is not enough information to generate significantly separate bimodal histograms to discriminate between sea ice and ocean. Also, because the antenna position in 2014 is not ideal for the Arctic, there is limited PWM data worth exploring.

It may be possible with further exploration in accounting for data gaps that PWM data could be found useful for sea ice extent measurements. However, with the development of the

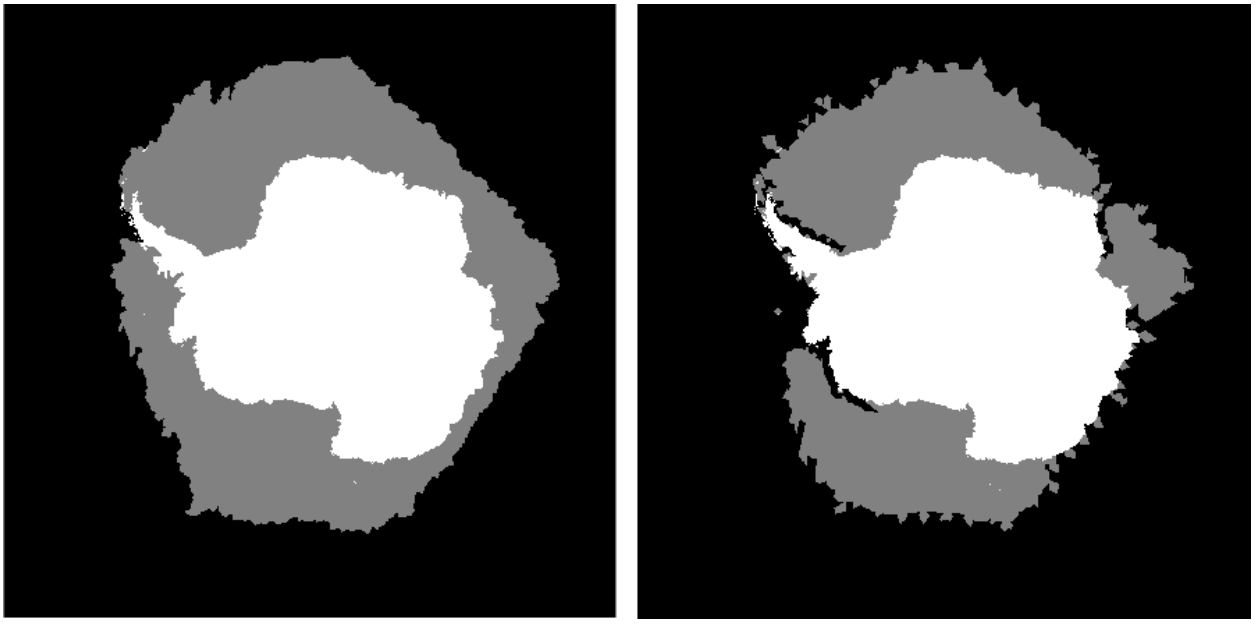

Figure A.5: Comparison of QuikSCAT ice masks: normal QuikSCAT data on day 201 of year 2009 (left) and QuikSCAT PWM data from days 201 to 210 of 2010 (right).

ASCAT sea ice extent algorithm, which processes data over the same time period as QuikSCAT PWM data, the QuikSCAT PWM sea ice extent experiment is determined not worth the investment of resources.